Dynamics of Aggregates and Sinking Carbon Fluxes in a Turbulent Ocean

Draft date: May 23, 2024

Authors: D.A. Siegel[1,*], A.B. Burd[2], M. Estapa[3], E. Fields[1], L. Johnson[4], E. Romanelli[1,5], M.A. Brzezinski[6], K.O. Buesseler[7], S. Clevenger[8], I. Cetinić[9], L. Drago[10], C.A. Durkin[11], R. Kiko[12], S.J. Kramer[11], A. Maas[13], M. Omand[14], U. Passow[15], and D.K. Steinberg[16]

1 - Earth Research Institute and Department of Geography, University of California, Santa Barbara, Santa Barbara, CA, USA, david.siegel@ucsb.edu & fields@ucsb.edu
2 - Department of Marine Sciences, University of Georgia, Athens, GA, USA, adrianb@uga.edu
3 - School of Marine Sciences, Darling Marine Center, University of Maine, Walpole, ME, USA, margaret.estapa@maine.edu
4 - Applied Physics Laboratory, University of Washington, Seattle, WA, leahjohn@uw.edu
5 - Institute of Environmental Engineering, Department of Civil, Environmental and Geomatic Engineering, ETH Zurich, Zurich, Switzerland, eromanelli@ethz.ch
6 - Marine Science Institute, University of California, Santa Barbara, Santa Barbara, CA, USA, mark.brzezinski@lifesci.ucsb.edu
7 - Department of Marine Chemistry & Geochemistry, Woods Hole Oceanographic Institution, Woods Hole, MA 02543, USA, kbuesseler@whoi.edu
8 - MIT-WHOI Joint Program in Oceanography, Applied Ocean Science and Engineering, Cambridge, MA, United States, samclev@mit.edu
9 - GESTAR II, Morgan State University, Baltimore, MD, USA and Ocean Ecology Laboratory, NASA Goddard Space Flight Center, Greenbelt, MD, USA, ivona.cetinic@nasa.gov
10 - Laboratoire d'Océanographie de Villefranche, Sorbonne Université, Paris, France and Sorbonne Université, UMR 7159 CNRS-IRD-MNHN, LOCEAN-IPSL, Paris, France laetitia.drago@imev-mer.fr
11 - Monterey Bay Aquarium Research Institute, Moss Landing, CA, USA, cdurkin@mbari.org & skramer@mbari.org,
12 - Laboratoire d'Océanographie de Villefranche, Sorbonne Université, Paris, France & GEOMAR Helmholtz Centre for Ocean Research, Kiel, Germany, rkiko@geomar.de
13 - Bermuda Institute of Ocean Sciences, School of Ocean Futures, Arizona State University, St. George's, Bermuda, amaas4@asu.edu
14 - Graduate School of Oceanography, University of Rhode Island, Narragansett, RI, USA, momand@uri.edu
15 - Ocean Sciences Centre, Memorial University Newfoundland, St. John's, NL, Canada & Marine Science Institute, University of California, Santa Barbara, Santa Barbara, CA, USA, uta.passow@mun.ca
16 - Coastal and Ocean Processes Section, Virginia Institute of Marine Science, William & Mary, Gloucester Point, VA, USA, debbies@vims.edu

*corresponding author

Abstract:

The ocean's biological pump, a critical component of the Earth's carbon cycle, transports organic matter from the surface ocean to depth, which is dominated by the sinking particles, often in the form of large (>1 mm) marine snow aggregates. Controls on carbon export are thought to be driven solely by ecological processes that produce and repackage sinking particles. Here, we present observations illustrating the important roles that storm-generated turbulence has on the abundance, characteristics and sinking fluxes of sinking particles. Turbulence creates and destroys aggregates and the vertical mixing induced by storms enhances their vertical transport. Evidence of the importance of biological processes is also observed. In all, these observations illustrate the complex interplay of physical and biological processes regulating the ocean's biological pump and the challenges in creating a predictive understanding of its function.

Teaser: The ephemeral nature of marine snow controls the sinking of carbon to depth and its contributions to the ocean's biological pump.

Short Title: On the ephemeral nature of marine snow and the ocean's biological pump

Keywords: Biological Carbon Pump, Marine Snow, Aggregate Dynamics, Ocean Turbulence, Sinking Carbon Export Fluxes

Introduction

The ocean's biological pump transports organic matter, created by phytoplankton productivity in the well-lit surface ocean, to the ocean’s dark interior, where it is consumed by animals and heterotrophic microbes and remineralized back to inorganic forms (1–3). This downward transport of organic matter, dominated by the gravitational settling of particles, sequesters respired carbon dioxide from exchange with the atmosphere on timescales of months to millennia, depending on the depth at which remineralization occurs and on ocean circulation and mixing processes (4,5). A predictive understanding of the biological pump function is critical to assess its role on future climate states and to measure the efficacy of carbon dioxide removal interventions aimed at contributing to net negative greenhouse gas emissions (6,7).

Much of what has been learned about the ocean's biological pump has come from field studies where the life cycle of particles is followed from their production in the upper ocean to their export to depth (1,8,9). The sinking speed of most particles (roughly 50 to 100 m d^{-1}) dictates a 5-to-10-day time scale to study the upper 500 m of the water column (estimated as the depth region of interest divided by a typical sinking time scale). Metrics for the efficiency of the biological pump, such as the e-ratio (export flux leaving the upper ocean divided by the net primary production, NPP), integrate biogeochemical fluxes over this time scale. The challenge arises when the biotic and abiotic factors vary on shorter time scales, such as during bloom events (10).

The rapid increase and subsequent decrease in phytoplankton biomass caused by the spring bloom in the subarctic oceans have long been of interest to oceanographers (11-15). The North Atlantic spring bloom is characterized by the dominance of siliceous diatoms followed by a transition to mixed flagellate communities as the diatom dominated biomass sinks out of the upper ocean (16,17). The relationship between primary productivity and sinking particle export is largely thought to be a balance between bottom-up and top-down controls (particle production vs. grazing) driven by the annual cycle of upper layer mixing (18,19). Here, we examine the demise of the North Atlantic spring bloom from the 2021 EXport Processes in the Ocean from RemoTe Sensing (EXPORTS-NA) field campaign and demonstrate that abiotic physical processes, occurring on synoptic time scales, can be the dominant factor regulating the gravitational component of the biological carbon pump.

Results

The Oceanographic Setting

The EXPORTS-NA field campaign was conducted within an anticyclonic eddy in the northeast Atlantic Ocean (20). An anticyclone was chosen as it would in principle retain water parcels within its core for the planned 25 days of sampling (21). Multiple sampling assets were deployed with the goals of understanding temporal changes within the eddy's core and assessing the spatial/temporal changes outside of it. The location of the eddy center was monitored using multiple methods and the success of this approach was verified using an instrumented, Lagrangian float that remained near the eddy center at depth of roughly 75 m throughout the cruise (20,21). Water property analyses showed that the eddy core waters (ECWs), within 15 km of the analyzed eddy center and below ~100 m, were retained throughout the experiment (20). However, above the eddy core, the surface core waters (SCWs) were subjected to a sequence of four intense storms (each with maximum hourly wind speeds exceeding 40 kts), which interrupted the ship-based sampling, deepened the mixed layer, and exchanged significant fractions of the SCWs with waters outside of the eddy due to Ekman transport (Figs. 1a & S1; 20).

Initially, the SCWs were characterized by extremely low silicate (SiO_4) (<0.4 μM), elevated nitrate (NO_3) (~5 μM; Fig. 1b), moderate chlorophyll *a* concentrations (~1.1 mg m^{-3}), and a dominance of microphytoplankton pigment biomarkers (~80% of the summed accessory pigment biomarkers; Fig. 1c). Together, this suggests that a bloom of diatoms had occurred previously and terminated due to SiO_4 limitation (22). Analysis of the upper ocean silica and nitrogen budgets indicates that ~70% of the diatom bloom had already been exported from the mixed layer before our arrival (22). The remaining nitrate supported the production of non-silicified phytoplankton during our field occupation and storm-induced, mixed layer entrainment supported intermittent diatom production (22,23; Fig. S2). This dual-phase bloom scenario is typical of the North Atlantic spring bloom (16). Thus, we here focus on the second phase of the spring bloom and its associated particle export.

Most surface layer biogeochemical variables were highest upon arrival at the eddy and decreased over time, including: chlorophyll *a*, particulate organic carbon (POC) and biogenic silica concentrations, the contribution of microphytoplankton pigments to accessory pigments, and water column integrated rates of net primary production (NPP) (20,22,23; Fig. 1c-e). Notably, vertically integrated rates of NPP decreased by >50%. The first storm event (May 7-11) had a large impact on the retention of SCWs and ~75% of these were exchanged with waters from outside of the eddy core region, while daily mean mixed-layer depths deepened from 22 to 68 m (20).

While NPP decreased two-fold in the field study, upper ocean sinking POC fluxes increased two-fold from the first to the third sediment trap deployments (Fig. 1e; Table S1). Comparing the POC flux at ~100 m to the POC stocks above it provides a measure of turnover of POC due to export from the upper ocean. These export turnover times were 2 to 3 months during the first two sediment trap deployments and about one month for the last. Turnover times for the production of POC (= POC inventory / NPP) were considerably shorter (1 to 2 weeks; Table S1), illustrating that much of the fixed organic carbon was utilized by the upper ocean ecosystem and not exported to depth. However, both lines of evidence suggest a residence time of upper ocean POC stocks of >1 week.

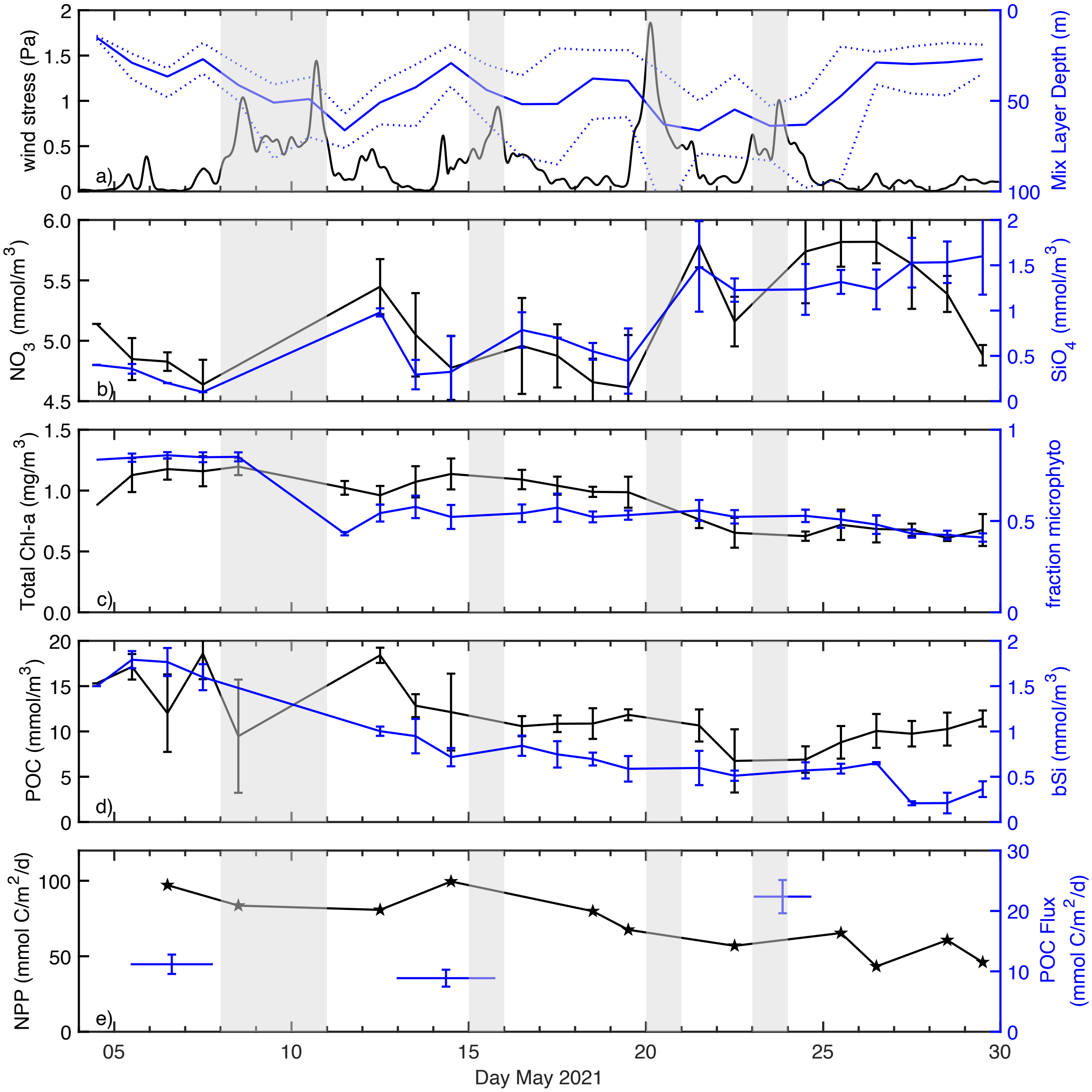

Figure 1: **Time series of oceanographic conditions in surface core waters during the EXPORTS-NA study**. Shown are time series of a) wind stress (black; left) and daily minimum, mean and maximum mixed layer depth (blue; right), b) mixed layer mean nitrate (NO_3; black; left) and silicate (SiO_4; blue right) concentrations, c) mixed layer daily mean total chlorophyll *a* concentrations (black; left) and fraction of microphytoplankton pigments of the summed accessory pigment biomarkers (blue; right; following ref. 24), d) mixed layer mean particulate organic carbon (POC; black; left) and biogenic silica (bSi; blue; right) concentrations and e) water column integrated rates of net primary production (NPP; black) and POC export fluxes measured at roughly 100 m using sediment traps (blue; right; see Table S1 for details). All measurements shown were made within 15 km of the eddy center. Error bars in panels b) to e) are standard deviation determinations for each daily mean or trap collection.

Distributions of Large Particle and Aggregates

Abundance-size distributions of large particles (~0.1 to 10 mm) were quantified as a function of depth using imagery collected by three Underwater Vision Profilers (UVPs; 25; *Methods*). Shown in Figure 2a are selected daily mean profiles of particle volume spectra presented in differential form. Initially, high volumes of particles smaller than 1 mm were found in the mixed layer while comparatively low particle volumes of any size were found at depth. From May 12-16, the maximum sizes of particles in the SCWs increased to greater than 3 mm, which may have been caused, at least in part, by horizontal exchanges of surface waters due to the storm-induced Ekman transport (Johnson et al. 2024). After May 15, a plume of large particles (>3 mm) appeared beneath the ML and over the next several days sank into the ECW. By May 25, the plume of large particles reached 500 m, implying an average sinking speed of ~33 m d^{-1} (300 m over 9 d). Post-bloom ecosystems in the North Atlantic often lead to rapid export of sinking particles from the surface ocean, but the delay between the first appearance of these particles in and just beneath the SCWs and their export was unexpected.

During the first 10 days of the study, daily mean particle volumes within the ECWs (depths ≥ 100 m) were relatively low and dominated by smaller particles (Fig. 2a). However, outside the eddy core at similar depths, significantly more and larger particles were observed (Fig. 2b). In particular, the particle volume spectra there were similar to those observed later in the study within the ECW (after May 22; Fig. 2a). This suggests that the midwater depths outside of the eddy core had already been modified by the passage of sinking particle plumes, while this signal was absent within the ECWs until after May 15. Midwaters outside of ECW were likely enhanced by lateral mixing from a patchwork of export flux events given the high degree of spatial heterogeneity in the surface biological fields (example daily mean satellite chlorophyll distributions are shown in Fig. S1). The low abundance of large particles within the ECW observed initially confirms the high degree of water parcel retention in the anticyclone's ECW (20). Importantly, the initial low particle volumes in the ECW provide a nearly pristine environment for diagnosing the dynamical relationships among particles and sinking particle fluxes.

The sinking speed estimate suggested from large particle plume can be refined to assess sinking speed as a function of particle size. Here, the sinking speed size distribution, $w_s(D)$, was determined by assessing temporal changes in the depth of particle abundance isosurfaces for each size bin (following ref. 26). Values of $w_s(D)$ increased with size and ranged from ~10 m d^{-1} to nearly 50 m d^{-1} for the largest particles assessed (Fig. 2c). These values correspond well with study mean estimates for fast-sinking particles determined from coordinated marine snow catcher (MSC) and sediment trap sampling (27) as well as theoretically derived sinking speed distributions (28).

Figure 2: **Vertical profiles of the particle volume size distribution for selected days**. a) Daily mean, differential particle volume spectra (ppmV/mm) profiles for selected days during the cruise and within 15 km of the eddy center. Particle volume spectra are presented in differential form as they accentuate changes in the particle size spectra that are difficult to visualize using particle abundance spectra. Bins are logarithmically distributed with bin centers from 0.13 to 10.3 mm. The black line denotes the daily mean MLD near the eddy center, while the gray line denotes the depth of the daily mean 27.2 kg m^{-3} isopycnal, which defines the upper boundary of the ECW (ref. 20). The storm icons denote the four storm periods with intense winds and waves and interruption of the ship-based sampling. The number in the lower left corner of each spectrum profile is the number of UVP casts used to create the daily mean shown. b) Daily mean particle volume spectra (ppmV/mm) profiles for selected days outside the eddy (15 to 60 km from eddy center). c) Mean particle sinking speed size distribution from following UVP particle abundance isosurfaces (black solid line); the standard deviation of the sinking speed estimates (gray shading); and two widely applied $w_s(D)$ estimates (dashed lines; entries 8 & 9 in Table 2 in ref. 28).

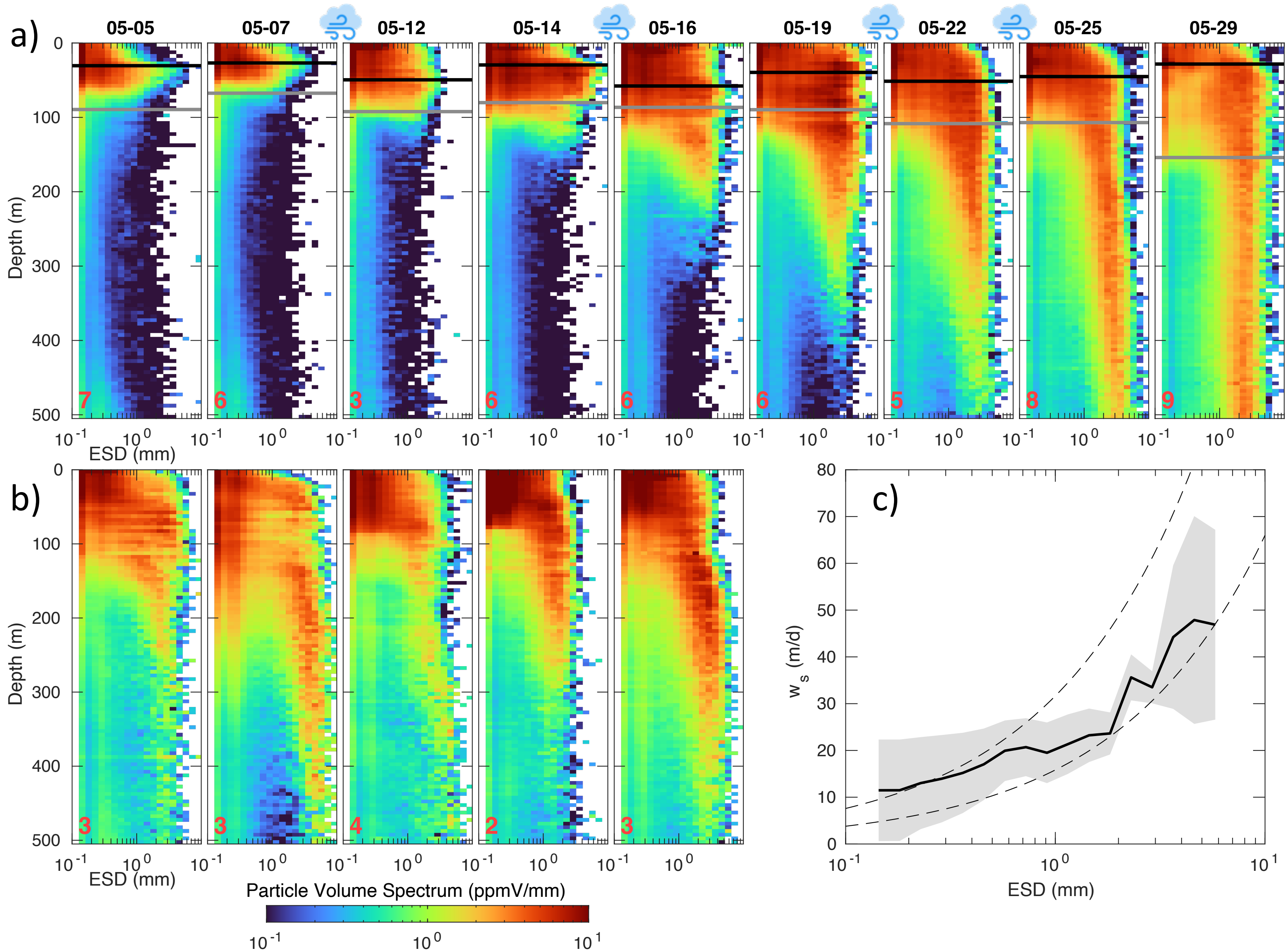
a)
05-05
05-07
05-12
05-14
05-16
05-19
05-22
05-25
05-29
Depth (m)
ESD (mm)
b)
c)
w_s (m/d)
Particle Volume Spectrum (ppmV/mm)

213

Structural Characteristics of the Large Particles Distribution

Knowledge of the physical structure of a particle is important for assessing its interactions with the environment and the organisms therein (3,29,30). Micrographs of sediment trap contents (Fig. 3a) show that large particles became more numerous, increased in size, became fluffier. Further, the trap collection periods decreased in the three trap deployments, indicating that the flux of large particles increased dramatically over the course of the study. These findings were corroborated by MSC observations (27) of increased aggregate abundances after May 12 and a higher number of large (>0.1 mm), fast-sinking aggregates over time and with depth (Fig. 3b). Daily mean aggregate abundances, determined via automated classification of individual UVP thumbnail images (see *Methods*), are consistent with the MSC results (Fig. 3b). Abundances of UVP-imaged aggregates show a similar increase after May 13 (Fig. 3c) and peak concentrations after May 24. Overall, more than 90% of the large particles (>1 mm) characterized from the individual UVP images were identified as aggregates. The correspondence between the three methods is reassuring, considering they quantify aggregates differently, either imaged from the bottom of a sediment trap, collected in a tray at the bottom of a marine snow catcher, or imaged *in situ*.

Large particles were extremely porous throughout the time series with solid particle fractions (defined as 1–porosity) ranging from 10^{-2} to 10^{-6} (Fig. 3c). This range of solid particle fractions is similar to previous in situ field determinations (31); however, the entire previously reported range was observed during our study. Values of solid particle fraction decrease in time, but no obvious changes in its depth distribution were found (Fig. 3c). Particle solid fractions were estimated by two methods: from sediment trap samples that collect sinking particles and from large volume pump-UVP pairings that sample water column particles (see *Methods*). Determinations of the solid particle fraction were higher for the sinking particles captured in traps than for particles imaged in the water column as expected; but both estimates decreased in time, indicating that the population of particles examined were becoming more porous (Fig. 3c). The extreme particle porosity observed indicates that the fractal nature of imaged particles must be considered in the quantitative analysis of particle mass using particle imaging tools (29,32,33).

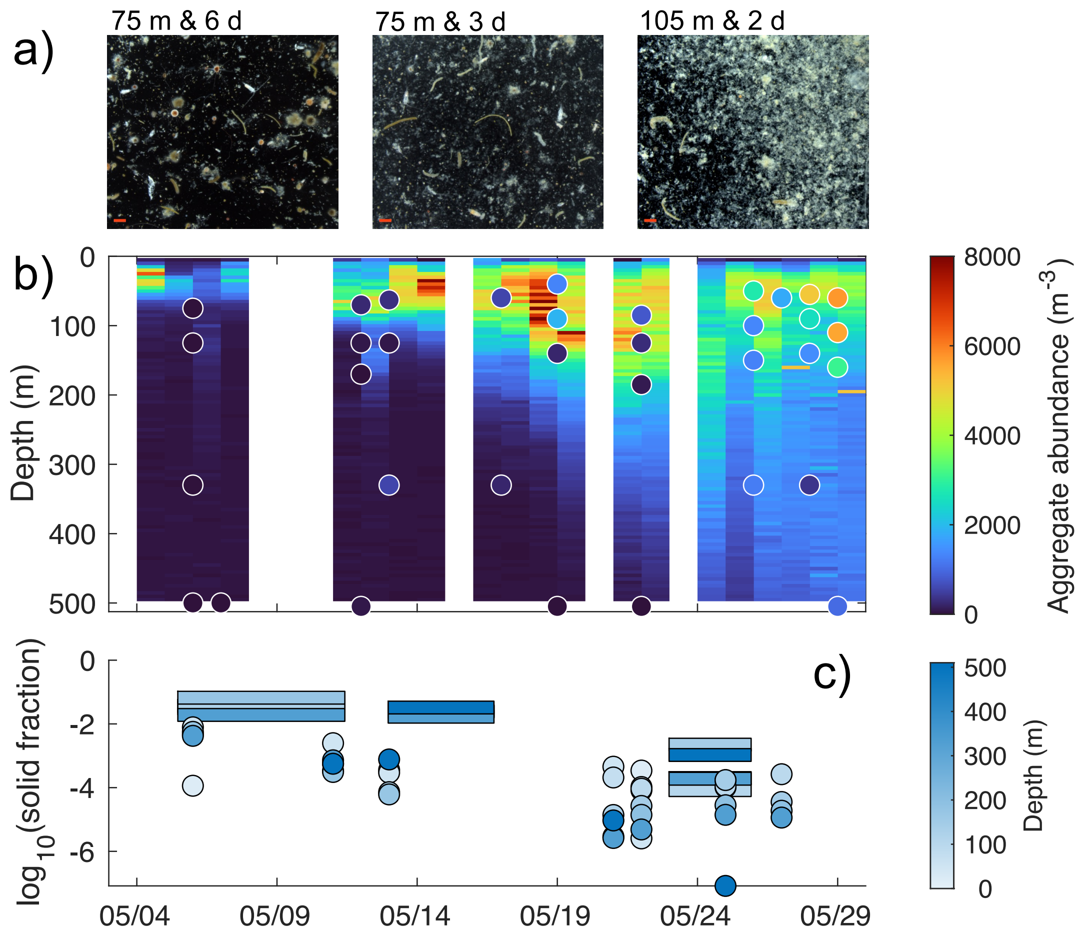

Figure 3: Structural changes in large particle characteristics in time and depth. a) Representative micrographs of gel trap contents from the three sediment trap deployments for size range of 50 µm to 5 mm. Scale bars in lower left corners of images (red) are 1 mm. Sampling depths and durations were 75 m and 6 days, 75 m and 3 days, and 105 m and 2 days for the three collection periods. b) Aggregate abundance and composition determinations as function of depth and time within the eddy center. UVP imaged aggregate abundance analysis are the contours, while fast sinking, large aggregates hand collected from the MSC collections are the filled circles. c) Solid particle fractions from geochemical/gel trap pairings (rectangles for which length denotes the trap collection duration) and high-volume pump and UVP matchups (circles). Depth of sample collections is shown in the color scale.

Abiotic Controls on Aggregates in the Surface Layer

Our observations reveal several examples where physical processes have proximate controls on the dynamics of large particles. For example, large reductions in particle volume and particle sizes are seen within the mixed layer close to the sea surface where turbulence levels are highest (Figs. 2a & S4). This is particularly evident on May 14, 22, and 25, when wind stress and thereby near surface turbulence levels were elevated (Fig. 1a). Turbulent shear rates are important for particle dynamics, as a moderate amount facilitates collisions among particles and promotes increases in particle sizes via shear coagulation, while high turbulence levels disaggregate particles (34-36). Relating the largest particle size (D_{max}) reliably sampled by the UVP (*Methods*) to turbulence levels within the mixed layer clearly shows the influence of mixed-layer turbulence on particle sizes. Over the entire study, maximum particle sizes within the mixed layer increased more than three-fold with depth, while turbulent kinetic energy dissipation rate, KE_{diss}, estimated from air-sea momentum and buoyancy fluxes (*Methods*), decreased rapidly (Fig. 4a). Maximum particle sizes are regulated, at least in part, by shear disaggregation due to elevated turbulence levels (34,36) as evidenced by the decrease in maximum particle sizes with KE_{diss} when $KE_{diss} > 10^{-7}$ W kg^{-1}. Maximum particle sizes observed were only rarely reached the maximum aggregate size found in the laboratory experiments of ref. (34) (blue line in Fig. 4b). Classic turbulence scaling predicts mixed-layer turnover times of an hour or less (scaling as Z_{ML} / u*, where Z_{ML} is the mixed-layer depth, u* is the surface friction velocity = $(\tau/\rho)^{1/2}$; τ is wind stress and ρ is seawater density); therefore, shear fragmentation must occur very quickly. Whereas turbulence levels near the surface favor smaller maximum particle size and fragmentation, those near the base of the mixed layer favor coagulation and larger particles. The largest particles were found at depth for intermediate values of KE_{diss} (Fig. 4b), suggesting that there is a turbulence level, roughly 5×10^{-8} W kg^{-1}, large enough to promote particle-particle encounters leading to coagulation, but not so large as to lead to disaggregation of those particles.

Over the study, daily mean estimates of KE_{diss} averaged over the upper 50 m of the water column varied by more than three orders of magnitude due to the presence or absence of storms (Fig. 4c). As a result, particles larger than 5 mm had a high potential for fragmentation during storm events, while they were more apt to grow during the quiescent periods between storms due to shear coagulation (Fig. 4c; see *Methods* for calculation details). The effects of the storms are evident in the upper layer integrated total particle volumes (Fig. 4d). Particle volumes were low just after each storm passed and then increased rapidly during more quiescent periods. After the first two storms (May 11-14 & May 16-19), total particle volumes increased nearly two-fold in just a few days. Changes in the upper-layer mean particle volume size spectra mirrored changes in the turbulence levels where particle sizes and volumes grew when turbulence levels were low and decreased when turbulence was high (Fig. 4e). This is reflected in temporal patterns in formation rates of particles > 5 mm by coagulation. Initially, upper-layer coagulation rates were small due to both low turbulence and a scarcity of particles that can coagulate into particles larger than 5 mm (Fig. 4e). After each storm, particle coagulation rates for particles > 5 mm in size increased dramatically as the lower turbulence levels promoted coagulation and the production of particles large enough to coagulate to yet larger ones. Thus, the dynamics of upper layer large particles (> 5 mm) is driven by fragmentation when turbulence is high (upper layer mean KE_{diss} greater than about 10^{-6} W kg^{-1}) and coagulation when turbulence levels are lower (Fig. 4c).

Together, these data illustrate the highly ephemeral nature of large aggregates in the upper ocean as perturbed by intense storm conditions.

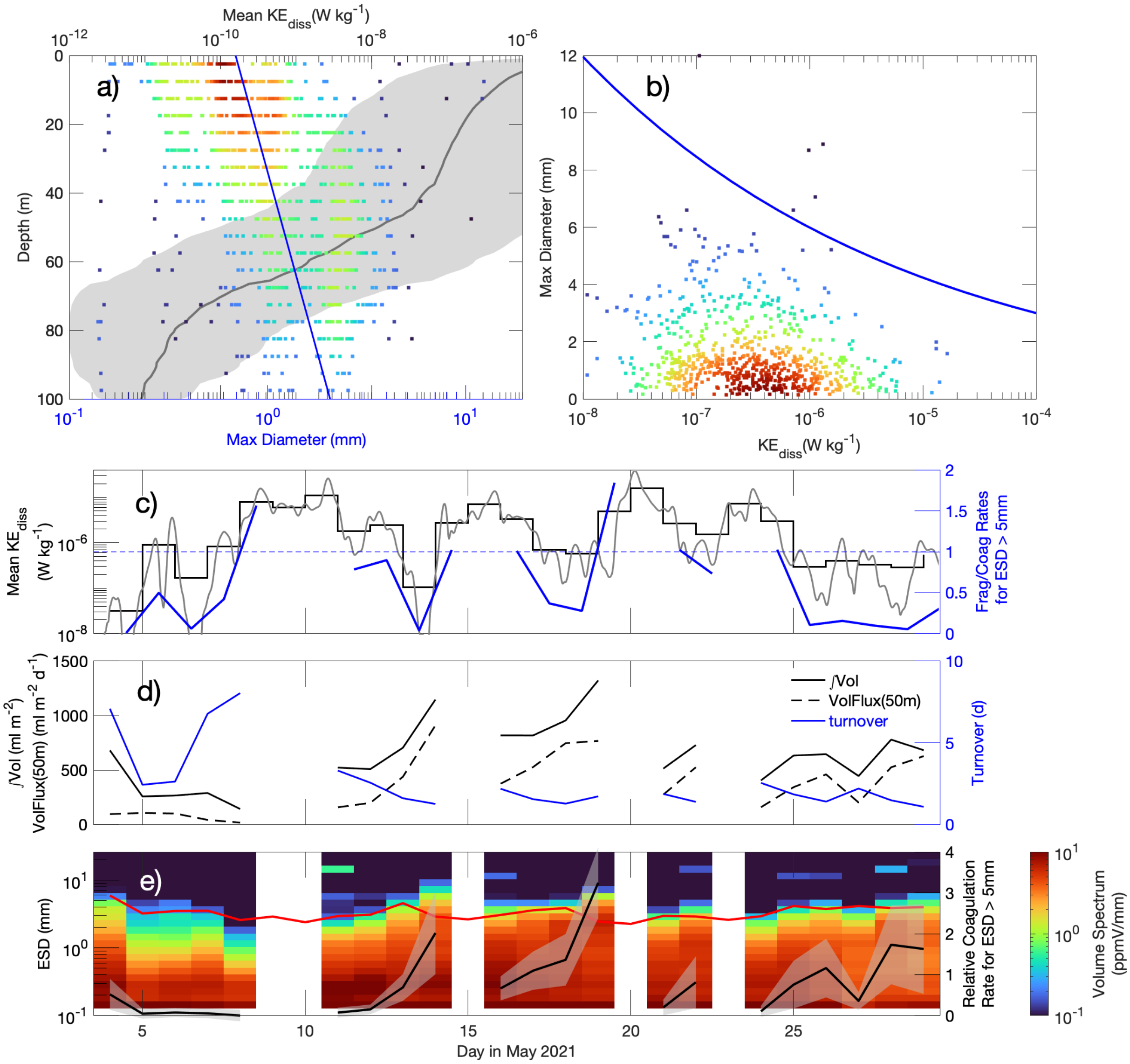

Figure 4: Turbulence and large particle dynamics in the upper 50 m. a) Individual observations of the maximum particle size, D_{max}, sampled by the UVP vs. depth within the mixed layer (see *Methods* for how D_{max} is estimated). Individual UVP observations and hourly KE_{diss} estimates are shown where the color represents the data density in D_{max}-depth space (red highest, blue lowest). The solid blue line is the best fit line of D_{max} with depth. The black line and gray envelope are the study mean and standard deviation envelope for the KE_{diss} vertical profile within the mixed layer. b) Comparison of individual D_{max} observations with KE_{diss} estimates. Data are the same as in a). The color for each observation represents the data density in KE_{diss}-depth space (again, red is highest). Blue solid line is the average maximum aggregate size found in the laboratory study ($D_{max} = 0.75\ (KE_{diss})^{-0.15}$; ref. 34). c) Time evolution of the mean KE_{diss} in the upper 50 m (black; hourly & daily) and the ratio of modeled particle fragmentation to particle growth via coagulation for particles larger than 5 mm (blue line; > 1 fragmentation dominates &

< 1 coagulation). d) Total particle volume inventory, particle volume sinking flux at 50 m and their turnover time. e) Upper 50 m mean particle volume spectra as function of time. Black lines are modeled time series of relative coagulation rates for large particles in the upper 50 m. The uncertainty envelope for coagulation rates illustrates the variations in the ensemble created using a range of fractal dimension scenarios. Also plotted (red line) is the maximum marine snow size as function of upper layer KE_{diss} based upon the laboratory experiments of ref. (34).

The storm events also influenced large particle dynamics by rapidly altering the depth of the surface mixed layer, which in turn impacted the vertical transport of large particles (Fig. 1a). As noted above, a pulse of sinking particles was observed traversing from the base of the mixed layer starting on May 14 and reaching 500 m on about May 25 (Fig. 2a). However, it is not clear what drove the timing of the sinking particle flux event. Initially (May 7), the UVP-imaged particle volume spectra showed very few particles > 1 mm below the mixed layer (Fig. 2a). After the first storm (May 12 and 14), larger particles were observed both within the mixed layer, but also below this depth (to ~80 m). The first storm not only exchanged SCWs with waters from outside the eddy, but it also deepened the mixed layer from 22 to 68 m (20; Fig. 5a). After the storm passed, the mixed layer shoaled rapidly, effectively exporting particles beneath the shallower mixed layer into the depth interval from 22 to 68 m, in a process similar to the seasonal mixed layer pump (37). Evaluating this for all storm events, both particle sizes and total particle volume between the depth interval from 40 to 80 m rapidly increased in between storms (Figs. 5a & b). Temporal patterns in the relative coagulation rates of large particles (> 5 mm) for the 40 to 80 m layer support the idea that coagulation was a significant driver of this increase (Fig. 5b).

The coupled turbulent and particle dynamics provide an explanation for the timing of the pulse of sinking large particles. Initially, large (> 5 mm) particle coagulation rates were extremely low in the 40 to 80 m layer. After the first storm, these rates increased rapidly as the abundance of particles available to make large aggregates increased, due to mixed layer pumping as well as via coagulation due to the moderate turbulence levels. These large particles then sank at velocities of order 50 m d^{-1} (Fig. 2c), sinking into the ECWs as can be seen on May 12 and 14 (Fig. 2a). The following storm, on May 15, accelerated this process. The large observed particle export pulse resulted from a complex combination of processes, including mixed layer entrainment and detrainment transporting large particles to depth, shear coagulation creating larger particles, and finally their sinking into the eddy interior.

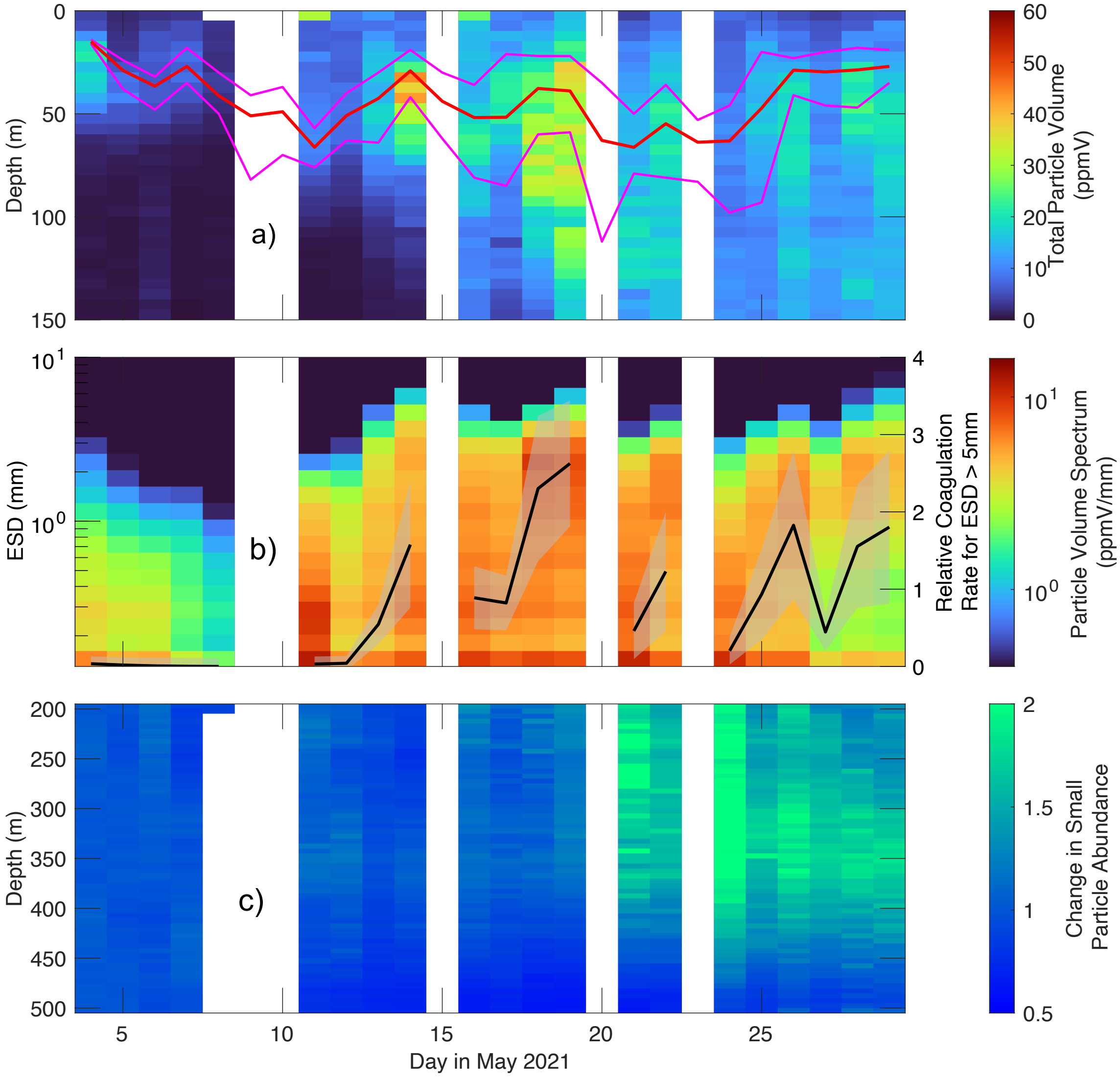

Figure 5: Dynamics of large particles at depth. a) Total particle volume depth-time series from the large (> 0.1mm) particle imagery (ppmV). Shown also in the red and pink lines are the daily minimum, mean, and maximum mixed layer depths from the instrumented glider which profiled roughly every two hours near the eddy center (20). b) Daily mean particle volume spectrum averaged for the layer between 40 to 80 m as a function of particle size. Overlayed are modeled time series of relative coagulation rates for large particles in the same layer where the uncertainty envelope illustrates the variation in the ensemble created using different fractal dimension scenarios. c) Relative changes in the vertical profile of the abundances of small particles (0.13 > D > 0.51 mm) with depth and time relative to the mean profile from May 4 and 5.

Last, repeated storm forcing suggests there was a successive reworking of particles in the upper ocean leading to increased particle porosity in time. This may have led to the explosive growth of large aggregates (> 5 mm) later in the study. Evidence for this can be found by evaluating the turnover time scales for POC and particle volumes in the upper 100 m of the water column. Turnover time scales for POC production

(∫POC/NPP) were about a week or two, while turnover time estimates for POC export were months (Table S1). Contrasting this, turnover times for large particle volumes (∫Vol/VolFlux(100m)) were about a week at the beginning of the cruise and decreased to about a day (Table S1). This implies that large particles were being rapidly created and exported, yet most of the particle mass, as measured by the POC concentration, was retained in the upper ocean. In fact, more than 90% of the POC in the MSC collections was found in the suspended fraction (27).

We suggest that the processes of sequential building and destroying of aggregates in the mixed layer may lead to a pool of particles whose porosity increases over time. Turbulence limits the size of aggregates by shearing them into two or more fragments by the smallest eddies in the flow, the Kolmogorov scale (34,36). Laboratory experiments on marine aggregates show that individual shear disaggregation events result in pairs of fragment particles most of the time (34,38). These fragments should have a similar fractal nature to their parent and when coagulated again, the resulting aggregates should become even more fractal and more porous. This hypothesis is consistent with observations of particle porosity growing over time during the experiment (Fig. 3c).

Aggregate Dynamics and Sinking Particle Carbon Export

Changes in the particle size distribution illustrate a net transport of large particles to depth (Fig. 2a) and likely an export of organic carbon to depth. However, given the large degree of porosity and its changes over time (Fig. 3c), correspondence between imaged particles and sinking POC fluxes is not guaranteed. Here, we compare estimates of sinking particle volume fluxes, determined from the imaged large particle distribution and an assumed sinking particle velocity size distribution (see *Methods*), to traditional measurements of sinking particle export.

Sinking particulate organic carbon (POC) fluxes were determined directly using surface tethered and neutrally buoyant sediment traps, as well as by several other tools that provide indirect or proxy flux determinations (Fig. 6). These include optical sediment traps, globally calibrated to provide estimates of sinking POC fluxes (OST-POC; 39), a prototype, upward-viewing time lapse camera mounted on the Lagrangian float (SnoCAM), ^{234}Th-derived POC fluxes (40), analysis of the fast-sinking components of POC in the MSC collections (27), and determinations of the particle volume sinking flux from in situ particle imaging (see *Methods*). Sinking particle fluxes and their proxies all show similar patterns with increasing fluxes in time and this signal propagating to depth over time. Before May 16, sediment trap-measured POC fluxes were relatively low with strong attenuation beneath the mixed layer (Fig. 6b). From May 14 to May 23, these fluxes increase by a factor of two in the upper ocean and that increase propagates to depth and were also detected by the ^{234}Th-derived POC fluxes (Fig. 6a). Sinking particle fluxes determined from the MSC collections follow this same pattern, but show a dramatic increase in flux after May 25 reaching ~60 mmol-C m^{-2} d^{-1} in the upper layers (27). This late study increase is supported by ^{234}Th-derived POC fluxes at 95 m (40). The optical sediment traps and SnoCAM detected a large increase in particle export at ~80 m, matching the initial patterns detected in the UVP particle volume fluxes. However, flux determinations from the optical sediment traps and SnoCAM decreased sharply after May 23, potentially due to spatial heterogeneity in sinking fluxes and/or an under sampling by the small-cross section beam transmissometer in the case of the OST (39), and low sensitivity of the prototype SnoCAM to large, low fractal-dimension aggregates as were observed later in the study (Fig. 3bc).

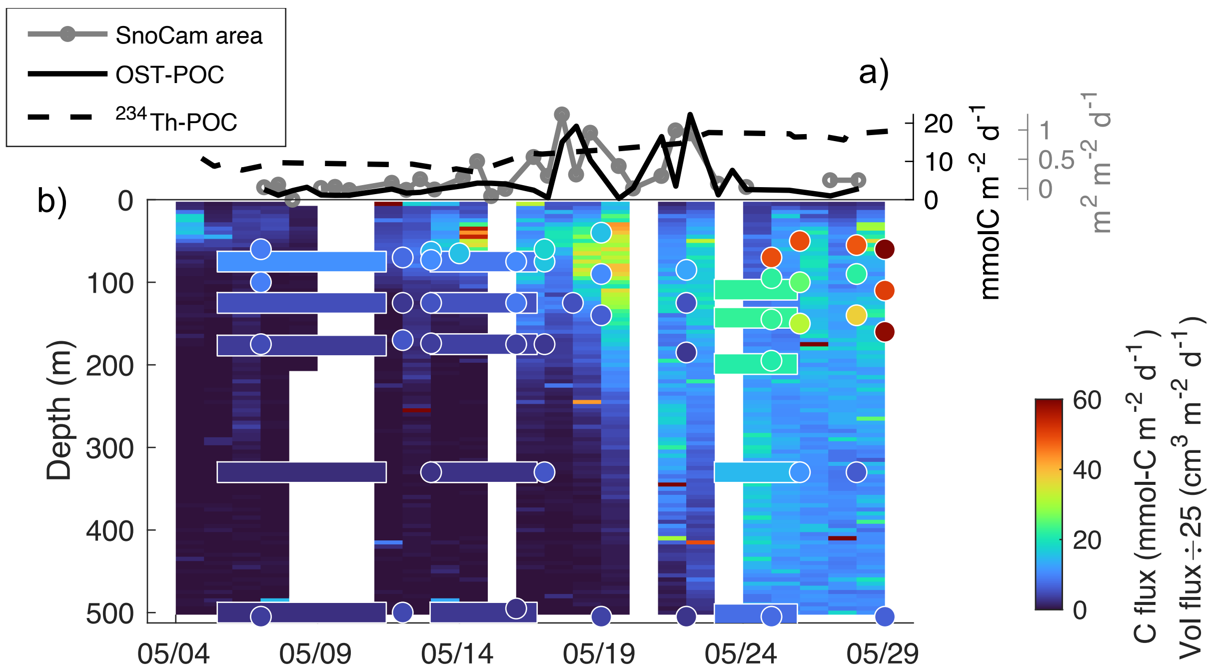

Figure 6: **Sinking POC fluxes and proxy measurements.** a) Sinking POC fluxes over time from different flux proxies. The black line shows the POC flux from the Optical Sediment Trap (OST); the brown line is the particle area flux sampled by the SnoCAM; and the black dashed line is the POC flux estimated from deficits of ^{234}Th at 75 m (Fig. 9 in ref. 40). The mean (± s.d.) depth of the OST and SnoCAM measurements was 75 ± 14 m. b) POC fluxes from geochemical sediment traps (rectangles), the marine snow catcher (circles) and UVP-determined particle volume flux estimates (contours). All measurements were made near the eddy center and are scaled to the common color bar.

Overall, particle dynamics and particle sinking determined from the time course of particle volume fluxes from UVP imagery correspond well with the POC export determined from the other approaches (Fig. 6b). The general increase in the sinking particle volume fluxes in both time and depth corresponds with the direct sinking POC fluxes and most of their proxies. Correspondence was also good with the MSC-derived POC fluxes, although the MSC fluxes are considerably higher in the upper 200 m late in the study and suggest lower flux transmission values. Although this is not a quantitative comparison of POC flux measurement methods (a subject of future work), it does support the use of particle imagery of large particle distributions for understanding vertical flux processes in the upper ocean.

Biotic Controls on Particles in the Upper Mesopelagic Zone

Apparent biotic controls on the particle size distribution can also be quantified in the upper mesopelagic zone of the eddy core waters. After May 20, abundance of small (≤ 0.51 mm) particles within the ECW increased by a factor of more than two compared to May 4-5 (Fig. 5c). It is unlikely these smaller particles sank from the surface ocean given the time required for these slow-sinking particles to traverse many 100's of meters (Fig. 2c). Horizontal advection can also be ruled out due to the retentive nature of the eddy and KE_{diss} levels are too low for significant shear disaggregation to occur. More likely, the observed increase in small particles is driven by biological processes, such as the destruction of large particles by zooplankton via sloppy feeding and/or animal-generated shears (41,42).

Support for this hypothesis can be found in estimates of the encounter rate between large (>0.51 mm) particles and zooplankton (see *Methods*). For the three days where simultaneous zooplankton and large particle data were available, estimated encounter rates increased by factors of 10 to nearly 30-fold from May 11 to May 26 (Table S2). This was due to a modest increase in zooplankton abundance (2x) and a strong increase in large particle abundances (>10x), consistent with the suggestion that the disaggregation of large particles by zooplankton created these smaller particles.

The imaged particle data can be used to quantify the rate of small particle (< 0.51 mm) production from large (≥ 0.51 mm) particles using a two size-class model of particle conserved volumes, which will be linearly related to particle biomass (44). The model (Eq. 1) relates the time rate of change of small and large particle conserved volumes to the sum of their sinking through the water column, the transformation of large particles to small ones with a specific rate β, and the consumptive losses of each with a specific rate γ, or

$$\frac{\partial P_S}{\partial t} = w_S \frac{\partial P_S}{\partial z} + \beta P_L - \gamma P_S \qquad (1a)$$

$$\frac{\partial P_L}{\partial t} = w_L \frac{\partial P_L}{\partial z} - \beta P_L - \gamma P_L \qquad (1b)$$

Large and small particle conserved volumes (and their gradients with respect to time and depth) were estimated via in situ particle imaging, with observed particle volumes converted to conserved volumes assuming an ensemble of particle fractal dimension values to account for particle porosity and its uncertainties. The model coefficients are determined by linear regression (see *Methods*).

The mean rate of transformation of large to small particles (β) is small (0.010 [0.006 s.d.] d^{-1}) yet positive for all ensemble members, demonstrating there is a net production of small particles from large ones. This estimated rate corresponds to nearly a 30% increase in small particle abundance for the 25-day experimental period, accounting for some, but not all of the observed, two-fold increase shown in Figure 5c. The net production of small particles from large ones occurs simultaneously with a large increase in zooplankton-to-large particle encounter rates (Table S2) suggesting that zooplankton-particle interactions, via zooplankton consumption, sloppy feeding, fragmentation by swimming action, or a combination thereof, is the likely source (41,44,45). Sloppy feeding will also enhance the solubilization of particles into dissolved forms which are widely available to the mesopelagic microbial community (46,47).

The two size-class model results also support several of our previous findings. For example, modeled large and small particle sinking speeds were 68.9 (2.7 s.d.) m d^{-1} and 12.1 (1.6 s.d.) m d^{-1}, respectively, consistent with assessments presented here (Fig. 1c) and study-mean determinations of sinking particle settling speeds made using paired MSC and sediment trap collections (27). The retrieved specific consumption rate (γ = 0.118 [0.008 s.d.] d^{-1}), is considerably higher than microbial O_2 consumption rates made on individual particles at this site (48), but it suggests that the consumption by grazers contributes substantially to particle losses.

Discussion

The observations presented here show that physical dynamics of the upper ocean can play a key role in particle transformations and the efficiency of sinking carbon export from the upper ocean. Mixed layer turbulence is required to produce and maintain a pool of marine snow aggregates that sink to depth, yet too much turbulence fragments them, thereby decreasing their sinking velocities and export potential. The passage of storms deepened the mixed layer, which rapidly shoals after the storms passed, leading to the isolation of particles roughly 30 m beneath the mixed layer. There, these particles were protected from the intense turbulent shear levels and the lower turbulence levels enabled increases in particle size through coagulation and thereby higher sinking rates. Last, the repeated storm forcings and turnover time scales for upper ocean POC and total particle volumes suggest a reworking of particles in the upper ocean leading to increasing particle porosity in time, which in turn may be related to the observed explosive growth of large aggregates (> 5 mm) late in the study. Together, these physical processes have a direct effect on particle size and sinking fluxes. They also influence the efficiency of the biological pump by increasing the residence times of particulate material in the upper layers, enabling more time for microbes and metazoans to remineralize and graze these particles. The net result of these competing processes will vary as a function of the coupling among food web, particle, and physical oceanographic dynamics, presenting a challenge for observing and modeling the mechanisms regulating important carbon cycling metrics, such as e-ratios and remineralization length scales.

We also show that biotic processes in the mesopelagic zone are disaggregating large (> 0.5 mm) particles into smaller ones (< 0.5 mm). This is likely related to the abundance and activity of zooplankton as other sources of these smaller particles within the ECWs seems unlikely. This supports recent studies suggesting that disaggregation processes are a critical component of flux attenuation with depth (47,49-51). Biological disaggregation is an important, yet poorly represented, process in models of the biological pump (3,52). Further, the production of small particles at depth provides a mechanism for their presence in sediment traps besides sinking from the sea surface (53). Thus, both abiotic and biotic particle aggregation and disaggregation processes need to be included in observational assessments and numerical models of the biological pump (8,52).

The sampling design for the EXPORTS-NA study leveraged the retentive nature of an anticyclonic eddy to enable observations of coupled ecological / biogeochemical processes in as close to a Lagrangian fashion as possible. The present observations of the large particle distribution inside and outside of the eddy core waters demonstrated that this goal was achieved, essentially separating temporal-vertical changes from lateral transport processes that would obscure signals of vertical export. This meant that the ECWs provided a near-pristine laboratory to understand the relationships among particle dynamics and sinking particles fluxes. In all, this work illustrates the importance of Lagrangian sampling designs to provide the required observational data for understanding the biological pump, particularly for sites with high eddy kinetic energy levels (8,20,54).

Last, there is a great deal of interest in the development of ocean-based carbon dioxide reduction (CDR) strategies to reduce atmospheric CO_2 levels (7). Measuring and validating the efficacy of a CDR action is critical for validating the carbon offsets its produces. Several biotic ocean CDR methods, such as ocean iron fertilization or artificial upwelling, attempt to intensify carbon export fluxes by spurring upper ocean NPP rates. Our work demonstrates that a complex combination of physical, biogeochemical and ecological processes will determine the fates of this enhanced carbon export and illustrates the complexity and challenges in monitoring and validating the additional carbon sequestered by the CDR action.

Methods and Materials

Experimental Array, Siting and Oceanographic Setting: The EXPORTS-NA field campaign was conducted ~150 km due east of the Porcupine Abyssal Plain (PAP) Observatory (55) in the northeast Atlantic Ocean within an anticyclonic eddy (20,21; Fig. S1). Three research vessels (RRS *James Cook*, RRS *Discovery* & R/V *Sarmiento de Gamboa*), three instrumented gliders, an instrumented Lagrangian float and 10 water following surface drifters were deployed during the experiment. The location of the eddy center was monitored by analyzing available horizontal velocity measurements from the multiple sampling assets and verified by the instrumented Lagrangian float that was deployed near the eddy center at depth of ~90 m (21). Measurements within 15 km of the analyzed eddy center were deemed in the eddy core based upon water property analyses. Below about 100 m, in the eddy core waters (ECWs), water parcels were retained within the eddy throughout the experiment (20). Thus, changes in biogeochemical and ecological properties in the ECWs were due to local processes and were independent of changes due to horizontal advection. However, in the surface core waters (SCWs) above the eddy, a series of four intense storms interrupted ship-based sampling (Fig. S1), deepened mixed layer depths and exchanged significant fractions of the upper water column (roughly 25 to 75%) due to Ekman transport (20).

Measurement Protocols: Measurement protocols for all measurements made during EXPORTS are available at https://sites.google.com/view/oceanexports. This includes the context variables presented in Fig. 1 for phytoplankton pigments, POC, and bSi concentrations, as well as 14-C NPP and sediment trap export fluxes.

Characterizing Large Particles using In Situ Imagery: Abundance and size of large particles and aggregates were quantified as a function of depth using the Underwater Vision Profiler 5 (UVP; 25) deployed from each of the three research vessels. The UVP illuminates approximately 1 L of seawater imaged at a pixel resolution of ~50 µm. Particles are identified as contiguous pixels whose area is converted equivalent spherical diameter. Particle abundance size distributions are then calculated for 25 logarithmically distribution bins with center bin diameters ranging from 0.09 to 23.9 mm. In standardizing the UVP data from the three ships, the first two bins were removed from consideration, making 0.13 mm the smallest particle diameter bin center reliably imaged (56). Particle abundance size distributions are averaged into 5 m vertical bins for equivalent spherical diameters ranging from 0.13 to 10 mm. Given the UVP's sampling frequency (6 Hz) and typical CTD frame lowering rates, nearly 100 individual scans make up each 5-m vertical average. This corresponds to each 5 m bin sampling ~100 L of seawater. Particle size spectra are reported here as particle volume spectra in differential form (units are ppmV per mm bin width) as they accentuate changes in the particle size spectra compared to visualizations made with particle abundance spectra and do not require the simultaneous reporting of bin dimensions (57,58). Further details including the standardizing of UVP particle size distribution observations from the three ships are included in ref. (56).

Total particle volumes are calculated as the integral of the differential particle volume spectra over the range of available diameters. Vertical sinking flux for particles is calculated as the integral of the daily mean differential particle volume spectra multiplied by an assumed sinking speed distribution over the diameters considered. Here, a theoretical sinking speed distribution from ref. (28) is used (their ref 8 in Table 2; the lower of the two curves presented in Fig. 2c). The size of the largest particles robustly sampled, D_{max}, is quantified as the largest differential particle volume threshold value that that is consistently well sampled by the UVP. A threshold value of 4 ppmV/mm provided consistent assessment of D_{max} for the mixed layer via experimentation with different thresholds.

Sinking speed size distributions were estimated from particle abundance distributions following ref. (26). For each size bin, particle abundance time-depth distributions were first smoothed and then 6 to 10 particle abundance isosurfaces are selected. The mean and standard deviation of the slope determinations of the depth-time relationships for the period May 14 to 25 are then calculated. Bin centers used range from 0.11 to 3.65 mm.

Aggregates abundances were quantified from an analysis of thumbnail images of large individual objects (> 1 mm). This classification was conducted first by using MorphoCluster (59), which enables the fast, human-assisted assimilation of likewise-appearing objects into clusters and subsequent classification. Thumbnails and their classification were uploaded to EcoTaxa (60) where classifications were further checked. Abundances of "fluffy" and "very fluffy" aggregates classified in this manner were binned together into 5 m vertical bins and daily averages (61).

<u>Sediment Trap Estimates of Sinking Particle Composition, Mass and Volume Fluxes:</u> Surface-tethered and neutrally-buoyant arrays of sediment traps were deployed three times during the cruise as described in refs. (39,62). Cylindrical trap tubes (0.0113 m^2) carried either poisoned brine (for bulk measurements of sinking POC, PIC, bSi, and mass flux) or polyacrylamide gel collectors (63) for particle enumeration, size, and classification. POC flux was determined following ref. (39). PIC flux was measured by coulometric analysis (64) on gravimetric splits of the same filters used for POC. Biogenic silica was measured by hot alkaline extraction of sample splits filtered onto polycarbonate membranes followed by spectrophotometric analysis (22). Gels were digitally imaged at 7x, 32x, and 115x magnification, then particles were identified and enumerated following methods in ref. (63). Image pixel size at 32x resolution was intercalibrated with the pixel size at 7x resolution following ref. (57). Particle diameter was used to estimate volume, assuming particles were spheres. Volume and mass fluxes were finally calculated by normalizing to trap deployment length and collection area. Surface tethered traps were subjected to horizontal velocities exceeding 30 cm s^{-1} and the upper trap briefly was within the surface mixed layer during Epoch 3, so only data from neutrally-buoyant sediment traps are shown in that Epoch.

<u>Marine Snow Catcher Assessments of Aggregate Abundances and POC Fluxes</u>: Sinking particles and sinking aggregates (ESD >0.1 mm) were collected below the mixed layer down to depths of 500 m using four Marine Snow Catchers (MSC) following methods in ref. (65). After retrieval, each MSC was placed on deck in an upright position for exactly 2 hours to allow the sinking of aggregates inside a circular plastic tray placed inside the base section of the MSC. Right after, the water collected in the base overlying the tray was gently sampled and the tray was transferred to the lab to manually pick individual aggregates (27). The aggregates were visually sized and counted. On May 27, the POC mass of the sinking aggregates was measured and used to calculate the POC concentration associated with the sinking aggregates (65). The base water and tray water (without the sinking aggregates) were processed to assess the POC concentrations of sinking particles. The sinking velocity of the entire sinking particle population (i.e., sinking particles plus sinking aggregates) was calculated by dividing the POC fluxes obtained from co-deployed sediment traps to the POC concentration of sinking particles

collected with the MSCs (27). Particle fluxes were calculated by multiplying the concentration of sinking particles by an estimate of their average sinking velocity.

Assessments of Solid Fractions of Sinking and Suspended Particles: Particle solid fractions were estimated as the ratio of solid particle component volumes to total particle volume. For sinking particles, measurements of bulk fluxes of POC, biogenic silica (bSi), and particulate inorganic carbon (PIC) (described above) were used to estimate the mass fluxes of organic matter, opal, and calcium carbonate, and representative component densities were then used to estimate the volume flux of the solid fraction in the particles (POC to organic matter [66]; bSi to opal [67]; PIC to $CaCO_3$, stoichiometry and densities; [68]). For suspended particles, a similar process was used to estimate the solid volume concentration from POC, bSi, and PIC concentrations measured in the > 335 µm size fraction of the large volume pump samples (40). For sinking particles, the total particle volume flux was estimated as described above, while for suspended particles, the volume concentration of ≥ 335 µm particles was estimated from UVP images. For both suspended and sinking particles, solid fractions were determined by dividing the corresponding solid volume by the total volume.

Estimation of Turbulent Kinetic Dissipation Rates from Air-Sea Flux Determinations: Turbulent kinetic energy dissipation rates (KE_{diss}; W kg^{-1}) were calculated for the upper 50 m of the water column using established similarity scalings (69,70), or

$$KE_{diss} = 0.58\left(-\frac{g\alpha Q}{\rho_o c_p} + g\beta(E-P)S_o\right) + \frac{1.76(\tau/\rho_o)^{3/2}}{\kappa z} \qquad \text{(M1)}$$

The first term represents the contribution from surface buoyancy forcing, where g is gravity, α is the thermal expansion coefficient, Q is the surface net heat flux, ρ_o is a reference density, β is the haline contraction coefficient, E is evaporation, P is precipitation and S_o is a reference salinity. The second term represents the contribution from momentum input, where τ is the surface wind stress, κ is the von Karmen constant, and z is depth from the surface. Surface heat and freshwater fluxes and wind stress were estimated using ship based meteorological measurements processed with the COARE bulk formula. Additional details can be found in ref. (20).

Modeling of Particle Coagulation and Disaggregation Rates: Particle coagulation rates are calculated using standard coagulation theory with a turbulent shear coagulation curvilinear kernel (29) using particle abundance and turbulent kinetic energy dissipation rates. Particle coagulation rates are calculated using a size-class based discretization from which total formation rates of large particles by coagulation are calculated (71). The UVP-determined ESD volume distributions are converted to conserved volumes (which is linearly related to particle biomass) ensuring total particle numbers remained the same (35). Large uncertainties exist for the fractal dimensions used for this conversion. Thus, an ensemble of simulations was created using a range of particle fractal dimensions from 1.5 to 2.3 covering a range of values from the literature (57,72-75). The ensemble included both particle fractal dimensions that are constant in time as well as examples that linearly decrease in time with initial and final values chosen randomly from above range. The final ensemble was made up of 21 members. Means and standard deviations of large particle formation rates by coagulation are calculated from the ensemble and shown in Figs. 4e and 5b.

Disaggregation rates of large particles are calculated following the model of Alldredge et al. (1990) (ref. 34). Maximum particle sizes are calculated as $D_{max} = 0.75\ (KE_{diss})^{-0.15}$. Conserved particle volumes in aggregates larger than D_{max} are redistributed into smaller particles such that 2/3 of the volume goes into the next size class smaller than the maximum particle size and the remaining volume is distributed uniformly among the smaller size classes.

Rates of large particle (> 5 mm) formation due to differential sedimentation were also determined (29). Conserved particle volume spectra were calculated as detailed above and particle sinking speed was calculated using Equation 8 of Table 2 in ref. (28) (the lower estimate in Fig. 2c). We find, for the 40 to 80 m layer where differential settlement should be more important, that shear coagulation rates are more than twelve times greater than differential sedimentation rates (Fig. S5). Hence, only rates of large particle formation due to shear coagulation are used in the qualitative discussions in the text.

Optical Sediment Trap and SnoCAM Sinking Particle Flux Determinations: Sinking particle fluxes were estimated at 75 m using two prototype tools for optical measurement of sinking particle fluxes that were both mounted on the instrumented Lagrangian Float deployed in the eddy core. A 25 cm beam transmissometer (~8 mm diameter collection area, C-Star, Sea-Bird Scientific Inc., Bellevue, WA) was used as an optical sediment trap (39) and collected data at an hourly frequency. A prototype upward-facing time-lapse camera (5 cm diameter collection area, SnoCam, University of Rhode Island) collected images of sedimenting particles at 4 hour intervals. For both instruments, particle flux was determined from the rate of signal increase over time. For the transmissometer-OST, POC flux was empirically estimated from beam attenuance flux (39). The SnoCam flux was reported as the rate of increase of particle projected area (mm^2 m^{-2} d^{-1}). The SnoCam imager was not optimized for sharp edge definition of porous, low fractal-dimension particles.

Radiochemical Assessment of POC Fluxes: Radiochemical assessment of POC fluxes via ^{234}Th measurements was carried out in accordance with the protocols described in ref. (76), wherein 2L seawater samples are precipitated with a MnO_2 coprecipitation method. Low-level beta decay activity (counts per minute) are then determined via counting on anti-coincidence beta decay counters (Risø DTU National Laboratory, Denmark). Thorium-234 fluxes (dpm m^{-2} d^{-1}; dpm = decays per minute) were analyzed using a non-steady state model (40). The non-steady state model assumes that the study system changes on a timescale less than the half-life of ^{234}Th (24.1 d). Thorium-234 fluxes were converted into POC fluxes by multiplying isotope fluxes by POC/^{234}Th ratios, collected using *in situ* pumps (40). Notably, POC fluxes included in this study are derived from the > 5 μm particle size class.

Large Particle-Zooplankton Encounter Rates: Encounter rates between zooplankton and large particles are estimated using a simple, geometric encounter rate. Zooplankton abundance (individuals m^{-3}) in 9 discrete depth intervals spanning 0-1000 m are calculated from MOCNESS net tows (three day-night pairs on May 11, 17, and 26) conducted in the eddy core. At sea samples from each depth interval were split using a Folsom plankton splitter and processed using protocols described in refs. (77,78). Half of the sample was size-fractionated using nested sieves (200, 500, 1000, 2000, and 5000 μm), rinsed onto pre-weighed 0.2 mm Nitex mesh filters, and frozen at -20°C for dry biomass analysis. The dry weight biomass of each size fraction for each depth interval (mg m^{-3}) was determined by dividing the biomass by the seawater volume filtered through the net. For the May 17 day-night pair, the other half of the sample was size-fractionated using the same nested sieves then preserved in sodium borate-buffered 4% formaldehyde. These preserved samples were imaged with a ZooSCAN version 3 at 2400 dpi (79). Briefly, at least 1500 particles per size fraction were scanned after subsampling using a Motoda splitter (80). Raw images were processed in ZooProcess (81,82), then uploaded to EcoTaxa (60) for machine assisted identification and then manually validated. This dataset provides the abundance of zooplankton from each size fraction from each depth interval after accounting for fraction imaged and volume filtered. By dividing measured dry mass from the equivalent sample by this measured abundance, we can calculate the average size of a zooplankton in that size fraction and net. We assumed the same average size organisms for the May 11 and 26 day-night pairs to calculate zooplankton abundance from these tows.

Encounter rates are estimated assuming zooplankton within each depth interval are uniformly distributed using large particle abundances from the UVP and particle sinking speeds from Fig. 1c. The encounter cross section between zooplankton and large particles is assumed to be 1 mm to take into account hydromechanical signal detection of particles by zooplankton (83).

Inverse Modeling Biotic Transformations of Small & Large Particles in the Mesopelagic: A simple inverse model (eq. 1) is used to assess the rates of transformation of large and small particle abundances in the mesopelagic via linear regression. The UVP-determined particle volume distributions are converted to conserved volumes following methods detailed previously. Mean values and gradients over both depth and time are then calculated using the daily mean observations of the small and large conserved volumes for six temporal intervals spanning different portions of the experiment and four 50 m vertical intervals. Linear regression analysis is then applied to estimate the four parameters in the inverse model. This is repeated for each member of the ensemble and uncertainties are assessed as the standard deviation of the ensemble of retrievals.

References:

1. Ducklow, H.W., D.K. Steinberg, K.O. Buesseler, Upper ocean carbon export and the biological pump. *Oceanography*, **14**, 50-58, (2001).
2. Le Moigne, F.A., Pathways of organic carbon downward transport by the oceanic biological carbon pump. *Front. Mar. Sci.*, **6**, 634, (2019).
3. Iversen, M.H., Carbon Export in the Ocean: A Biologist's Perspective. *Ann. Rev. Mar. Sci.*, **15**, 357-381, https://doi.org/10.1146/annurev-marine-032122-035153, (2023).
4. Nowicki, M., T. DeVries, and D.A. Siegel, Quantifying the carbon export and sequestration pathways of the ocean's biological carbon pump. *Glob. Biogeochem. Cyc.*, https://doi.org/10.1029/2021GB007083, (2022).
5. Siegel, D.A., T. DeVries, I. Cetinić, K.M. Bisson, Quantifying the Ocean's Biological Pump and its Carbon Cycle Impacts on Global Scales. *Ann. Rev. Mar. Sci.*, https://doi.org/10.1146/annurev-marine-040722-115226, (2023).
6. Henson, S.A., Laufkötter, C., Leung, S. *et al.* Uncertain response of ocean biological carbon export in a changing world. *Nat. Geosci.* **15**, 248–254, https://doi.org/10.1038/s41561-022-00927-0, (2022).
7. National Academies of Sciences, Engineering, and Medicine. *A Research Strategy for Ocean-based Carbon Dioxide Removal and Sequestration*. Washington, DC: The National Academies Press. https://doi.org/10.17226/26278, (2022).
8. Siegel, D. A., Buesseler, K. O., Behrenfeld, M. J., Benitez-Nelson, C. R., Boss, E., Brzezinski, M. A., et al., Prediction of the export and fate of global ocean net primary production: The EXPORTS science plan. *Front. Mar. Sci.*, **3**, https://doi.org/10.3389/fmars.2016.00022, (2016).

9. Buesseler, K.O., P.W. Boyd, E.E. Black, D.A. Siegel, Metrics that matter for assessing the ocean biological carbon pump. *Proc. Natl. Acad. Sci. U.S.A.*, **117**, 9679-9687, (2020).

10. Giering, S. L. C., R. Sanders, A.P. Martin, S.A. Henson, J.S. Riley, C.M. Marsay, D.G. Johns Particle flux in the oceans: Challenging the steady state assumption, *Glob. Biogeochem. Cyc.*, **31**, 159–171, https://doi.org/10.1002/ 2016GB005424, (2017).

11. Sverdrup, H.U., On conditions for the vernal blooming of phytoplankton. *J. Cons. Int. Explor. Mer*, **18**, 287-295, (1953).

12. Ducklow, H.W., R.P. Harris, Introduction to the JGOFS North Atlantic bloom experiment. *Deep Sea Research Part II*, **40**, 1-8, (1993).

13. Siegel, D.A., S.C. Doney and J.A. Yoder, The North Atlantic spring phytoplankton bloom in the and Sverdrup's critical depth hypothesis. *Science*, **296**, 730-733. https://doi.org/10.1126/science.1069174, (2002).

14. Behrenfeld, M.J., Abandoning Sverdrup's critical depth hypothesis on phytoplankton blooms. *Ecology*, **91**, 977-989, (2010).

15. Mahadevan, A., E. D'Asaro, C. Lee, M.J. Perry, Eddy-driven stratification initiates North Atlantic spring phytoplankton blooms. *Science*, **337**, 54-58 (2012).

16. Sieracki, M.E., P.G. Verity, D.K. Stoecker, Plankton community response to sequential silicate and nitrate depletion during the 1989 North Atlantic spring bloom. *Deep Sea Res. II*, **40**, 213-225, (1993).

17. Cetinić, I., M.J. Perry, E. D'Asaro, N. Briggs, N. Poulton, M.E. Sieracki, C.M. Lee, A simple optical index shows spatial and temporal heterogeneity in phytoplankton community composition during the 2008 North Atlantic Bloom Experiment, *Biogeosci.*, **12**, 2179–2194, https://doi.org/10.5194/bg-12-2179-2015, (2015).

18. Wassmann, P., Retention versus export food chains: processes controlling sinking loss from marine pelagic systems. *Hydrobiologia* **363:** 29–57, (1998).

19. Laurenceau-Cornec E.C., M. Mongin, T.W. Trull, M. Bressac, E.L. Cavan, L.T. Bach, et al., Concepts toward a global mechanistic mapping of ocean carbon export. *Global Biogeochem. Cyc.*, **37**, e2023GB007742. https://doi.org/10.1029/2023GB007742, (2023).

20. Johnson, L., D.A. Siegel, A.F. Thompson, E. Fields, Z.K. Erickson, I. Cetinić, I., et al., Assessment of oceanographic conditions during the North Atlantic EXport processes in the ocean from RemoTe Sensing (EXPORTS) Field campaign. *Prog. Oceanog.*, 103170, https://doi.org/10.1016/j.pocean.2023.103170, (2024).

21. Erickson, Z.K., E. Fields, L. Johnson, A.F. Thompson, L.A. Dove, E. D'Asaro, D.A. Siegel, Eddy tracking from in situ and satellite observations. *J. Geophys. Res.: Oceans*, **128**, e2023JC019701. https://doi.org/10.1029/2023JC019701, (2023).

22. Brzezinski, M.A., L. Johnson, M. Estapa, S. Clevenger, M. Roca-Martí, E. Romanelli, K.N. Buck, B.D. Jenkins and J.L. Jones, Physical mechanisms sustaining silica production following the demise of the diatom phase of the North Atlantic spring phytoplankton bloom during EXPORTS. In review at *Glob. Biogeochem. Cyc.*

23. Meyer, M.G., Brzezinski, M., Cohn, M.R., Kramer, S.J., Paul, N., Sharpe, G.C., et al., Primary production dynamics during the decline phase of the North Atlantic annual spring bloom. *bioRxiv*, https://doi.org/10.1101/2023.05.18.541304, (2023).

24. Uitz, J., H. Claustre, A. Morel, S.B. Hooker, Vertical distribution of phytoplankton communities in open ocean: An assessment based on surface chlorophyll. *Journal of Geophysical Research*, *111*(C08005), 1–23. https://doi.org/10.1029/2005JC003207, (2006).

25. Picheral, M., L. Guidi, L. Stemmann, D.M. Karl, G. Iddaoud, G. Gorsky, The Underwater Vision Profiler 5: An advanced instrument for high spatial resolution studies of particle size spectra and zooplankton. *Limnol. Oceanogr.: Methods*, **8**, 462-473, (2010).

26. Lacour, L., Llort, J., Briggs, N., Strutton, P.G. and Boyd, P.W., Seasonality of downward carbon export in the Pacific Southern Ocean revealed by multi-year robotic observations. *Nature Comm.*, **14**, p.1278, https://www.nature.com/articles/s41467-023-36954-7, (2023).

27. Romanelli, E., S.L.C. Giering, M. Estapa, D.A. Siegel, U. Passow, Intense storms affect sinking particle fluxes after the North Atlantic diatom spring bloom. *bioRxiv* 2024.01.11.575202; https://doi.org/10.1101/2024.01.11.575202, (2024).

28. Kriest, I., Different parameterizations of marine snow in a 1D-model and their influence on representation of marine snow, nitrogen budget and sedimentation. *Deep Sea Res. Part I*, **49**, 2133-2162. (2002).

29. Burd, A.B., G.A. Jackson, Particle aggregation. *Ann. Rev. Mar. Sci.*, **1**, 65-90, https://doi.org/10.1146/annurev.marine.010908.163904, (2009).

30. Laurenceau-Cornec, E.C., T.E. Trull, D.M. Davies, L. Christina, S. Blain, Phytoplankton morphology controls on marine snow sinking velocity. *Mar. Ecol. Prog. Ser.*, **520**, 35-56, (2015).

31. Alldredge, A.L., C. Gotschalk, In situ settling behavior of marine snow. *Limnol. Oceanogr.*, **33**, 339–351, (1988).

32. Logan, B.E., D.B. Wilkinson, Fractal geometry of marine snow and other biological aggregates. *Limnol. Oceanogr*. **35**, 130–136. doi:10.2307/2837345, (1990).

33. Stemmann, L., Jackson, G.A. and Ianson, D., A vertical model of particle size distributions and fluxes in the midwater column that includes biological and physical processes—Part I: model formulation. *Deep Sea Res, Part I:* **51**, 865-884, https://doi.org/10.1016/j.dsr.2004.03.001, (2004).

34. Alldredge, A.L., T.C. Granata, C.C. Gotschalk, T.D. Dickey, The physical strength of marine snow and its implications for particle disaggregation in the ocean. *Limnol. Oceanogr.*, ***35***, 1415-1428, (1990).

35. Jackson G.A., A model of the formation of marine algal flocs by physical coagulation processes. *Deep-Sea Res. A* **37**, 1197–211, (1990).

36. Takeuchi, M., M.J. Doubell, G.A. Jackson, M. Yukawa, Y. Sagara, H. Yamazaki, Turbulence mediates marine aggregate formation and destruction in the upper ocean. *Sci. Rep.* **9**, 16280, https://doi.org/10.1038/s41598-019-52470-5, (2019).

37. Dall'Olmo, G., J. Dingle, L. Polimene, R.J. Brewin, H. Claustre, Substantial energy input to the mesopelagic ecosystem from the seasonal mixed-layer pump. *Nature Geosci.*, **9**, 820-823, (2016).

38. Song Y., A.B. Burd, M.J. Rau, The deformation of marine snow enables its disaggregation in simulated oceanic shear. *Front. Mar. Sci*. 10:1224518, https://doi.org/10.3389/fmars.2023.1224518, (2023).

39. Estapa M.L., C.A. Durkin, W.H. Slade, C.L. Huffard, S.P. O'Neill, M.M. Omand, A new, global optical sediment trap calibration. *Limnology & Ocean Methods*: lom3.10592. https://doi.org/10.1002/lom3.10592, (2023).

40. Clevenger S.J., C.R. Benitez-Nelson, M. Roca-Martí, W. Bam, M. Estapa, et al., Carbon and silica fluxes during a declining North Atlantic spring bloom as part of the EXPORTS program. *Mar. Chem.* **258**, 104346. https://doi.org/10.1016/j.marchem.2023.104346, (2024).

41. Dilling, L., A.L. Alldredge, Fragmentation of marine snow by swimming macrozooplankton: a new process impacting carbon cycling in the sea. *Deep-Sea Res. I*, **47**, 1227‑1245, (2000).

42. Steinberg, D.K., M.R. Landry, Zooplankton and the ocean carbon cycle. *Annual Review of Marine Sciences*, *9*, 413-444, (2017).

43. Jackson, G.A., A.B. Burd, Simulating aggregate dynamics in ocean biogeochemical models. *Prog. Oceanog.*, **133**, 55–65, https://doi.org/10.1016/j.pocean.2014.08.014, (2015).

44. Dilling, L., J. Wilson, D. Steinberg, A. Alldredge, Feeding by the euphausiid, *Euphausia pacifica*, and the copepod, *Calanus Pacificus*, on marine snow. *Mar. Ecol. Prog. Ser.*, **170**, 189-20. DOI: 10.3354/meps170189, (1998).

45. Goldthwait, S., J. Yen, J. Brown, A. Alldredge, Quantification of marine snow fragmentation by swimming euphausiids, *Limnology and Oceanography*, **49**, 940-952, https://doi.org/10.4319/lo.2004.49.4.0940, (2004).

46. Møller, E.F., P. Thor, T.G. Nielsen, Production of DOC by *Calanus finmarchicus*, *C. glacialis* and *C. hyperboreus* through sloppy feeding and leakage from fecal pellets. *Mar. Ecol. Prog. Ser.*, **262**, 185–191, (2003).

47. Collins, J.R., B.R. Edwards, K. Thamatrakoln, J.E. Ossolinski, G.R. DiTullio, K.D. Bidle, S.C. Doney, B.A. Van Mooy, The multiple fates of sinking particles in the North Atlantic Ocean. *Glob, Biogeochem. Cyc.*, **29**, 1471-1494, (2015).

48. Belcher, A., M. Iversen, S. Giering, V. Riou, S.A. Henson, L. Berline, L. Guilloux, R. Sanders, Depth-resolved particle-associated microbial respiration in the northeast Atlantic, *Biogeosciences*, **13**, 4927–4943, https://doi.org/10.5194/bg-13-4927-2016, (2016).

49. Giering, S.L., R. Sanders, R.S. Lampitt, T.R. Anderson, C. Tamburini, M. Boutrif, M.V. Zubkov, C.M. Marsay, S.A. Henson, K. Saw, K. Cook, Reconciliation of the carbon budget in the ocean's twilight zone. *Nature*, **507**, 480-483, (2014).

50. Briggs, N., G. Dall'Olmo, H. Claustre, Major role of particle fragmentation in regulating biological sequestration of CO_2 by the oceans. *Science*, **367**, 791-793, (2020).

51. Giering, S.L.C., R. Sanders, S. Blackbird, N. Briggs, F. Carvalho, H. East, et al., Vertical imbalance in organic carbon budgets is indicative of a missing vertical transfer during a phytoplankton bloom near South Georgia (COMICS). *Deep Sea Res. Part II*, **209**, 105277, (2023).

52. Burd, A.B., Modeling the Vertical Flux of Organic Carbon in the Global Ocean. *Ann. Rev. Mar. Sci.*, **16**, https://doi.org/10.1146/annurev-marine-022123-102516, (2024).

53. Richardson T.L., G.A. Jackson, Small phytoplankton and carbon export from the surface ocean. *Science*, 315, 838-840, https://doi.org/10.1126/science.1133471. (2007).

54. Briggs, N., M.J. Perry, I. Cetinić, C. Lee, E. D'Asaro, A.M. Gray, E. Rehm, High-resolution observations of aggregate flux during a sub-polar North Atlantic spring bloom. *Deep-Sea Res. Part I*, **58**, 1031-1039, (2011).

55. Hartman, S.E., B.J. Bett, J.M. Durden, S.A. Henson, M. Iversen, et al., Enduring science: three decades of observing the Northeast Atlantic from the Porcupine Abyssal Plain Sustained Observatory (PAP-SO). *Prog. Oceanogr.*, **191**, https://doi.org/10.1016/j.pocean.2020.102508, (2021).

56. Siegel, D.A., I. Cetinić, A.F. Thompson, N.B. Nelson, M. Sten, et al., EXport Processes in the Ocean from RemoTe Sensing (EXPORTS) North Atlantic sensor calibration and intercalibration documents. https://doi.org/10.1575/1912/66998, (2023).

57. Jackson, G.A., R. Maffione, D.K. Costello, A.L. Alldredge, B.E. Logan, H.G. Dam, Particle size spectra between 1 μm and 1 cm at Monterey Bay determined using multiple instruments. *Deep-Sea Res. I*, 44:1739–1767, (1997).

58. Zhang, X. Y. Huot, D. Gray, H.M. Sosik, D. Siegel, L. Hu, et al., Particle size distribution at Ocean Station Papa from nanometers to millimeters constrained with intercomparison of seven methods. *Elem. Sci. Anth.,* **11** (1): 00094. https://doi.org/10.1525/elementa.2022.00094, (2023).

59. Schröder, S.M., Kiko, R. and Koch, R., 2020. MorphoCluster: Efficient annotation of plankton images by clustering. *Sensors*, **20**, 3060. https://doi.org/10.3390/s20113060, (2020).

60. Picheral, M., S. Colin, J.O. Irisson. EcoTaxa, a tool for the taxonomic classification of images. https://ecotaxa.obs-vlfr.fr/, (2017).

61. Drago, L., Analyse globale de la pompe à carbone biologique à partir de données en imagerie quantitative. Biodiversité et Ecologie. Sorbonne Université, 2023. Français. ⟨NNT : 2023SORUS562⟩. ⟨tel-04483392⟩, (2023).

62. Estapa M.L., K. Buesseler, C.A. Durkin, M. Omand, C.R. Benitez-Nelson et al. Biogenic sinking particle fluxes and sediment trap collection efficiency at Ocean Station Papa. *Elem. Sci. Anth.,* **9**, 00122, https://doi.org/10.1525/elementa.2020.00122, (2021).

63. Durkin C.A., K.O. Buesseler, I. Cetinić, M.L. Estapa, R.P. Kelly, M. Omand, A visual tour of carbon export by sinking particles. *Glob, Biogeochem. Cyc.*, **35**, e2021GB006985. https://doi.org/10.1029/2021GB006985, (2021).

64. Honjo S., R. Francois, S. Manganini, J. Dymond, R. Collier, Particle fluxes to the interior of the Southern Ocean in the Western Pacific sector along 170.3W. *Deep Sea Res. Part II*, **47**: 3521–3548, (2000).

65. Romanelli, E., J. Sweet, S.L.C. Giering, D.A. Siegel, U. Passow, The importance of transparent exopolymer particles over ballast in determining both sinking and suspension of small particles during late summer in the Northeast Pacific Ocean *Elem. Sci. Anth.,* **11**, 00122. https://doi.org/10.1525/elementa.2022.00122, (2023).

66. Lam P.J., S.C. Doney, J.K.B. Bishop, The dynamic ocean biological pump: Insights from a global compilation of particulate organic carbon, $CaCO_3$, and opal concentration profiles from the mesopelagic. *Glob, Biogeochem. Cyc.*, **25**, doi: 10.1029/2010GB003868, (2011).

67. Mortlock R.A., P.N. Froelich, A simple method for the rapid determination of biogenic opal in pelagic marine sediments. *Deep Sea Res. Part A,* 36(9): 1415–1426. doi: 10.1016/0198-0149(89)90092-7, (1989).

68. Laurenceau-Cornec, E.C., Le Moigne, F.A., Gallinari, M., Moriceau, B., Toullec, J., et al., New guidelines for the application of Stokes' models to the sinking velocity of marine aggregates. *Limnol. Oceanogr.*, *65*(6), 1264-1285. https://doi.org/10.1002/lno.11388, (2020).

69. Lombardo, C.P., M.C. Gregg, Similarity scaling of viscous and thermal dissipation in a convecting surface boundary layer. *J. Geophys. Res.: Oceans*, **94**(C5), 6273-6284, (1989).

70. D'Asaro, E.A., Turbulence in the upper-ocean mixed layer. *Ann. Rev. Mar. Sci.*, **6**, 101-115, (2014).

71. Burd, A.B., Modeling particle aggregation using size class and size spectrum approaches. *J. Geophys. Res. Oceans*, **118**, 3431–3443, https://doi.org/10.1002/jgrc.20255, (2013).

72. Logan, BE, A.L. Alldredge, The increased potential for nutrient uptake by flocculating diatoms. *Mar. Biol.*, **101**, 443–450, (1989).

73. Li, X., B.E. Logan, Size distributions and fractal properties of particles during a simulated phytoplankton bloom in a mesocosm. *Deep-Sea Res. II*, 42:125–138, (1995).

74. Risović, D., M. Martinis, Fractal dimension of suspended particles in seawater. *J. Coll. Interf. Sci.*, **182**,199–203, (1996).

75. Ploug, H., M.H. Iversen, G. Fischer G., Ballast, sinking velocity, and apparent diffusivity within marine snow and fecal pellets: Implications for substrate turnover by attached bacteria. *Limnol. Oceanogr.*, 53:1878–1886, (2008).

76. Clevenger S.J., C.R. Benitez-Nelson, J. Drysdale S. Pike, V. Puigcorbé, K.O. Buesseler, Review of the analysis of ^{234}Th in small volume (2-4L) seawater samples: improvements and recommendations. *J. Radioanal. Nucl. Chem*. **329**, 1-13, (2021).

77. Steinberg, D. K., J. S. Cope, S. E. Wlson, and T. Kobari (2008) A comparison of mesopelagic mesozooplankton community structure in the subtropical and subarctic North Pacific Ocean. *Deep-Sea Research II* 55(14-15): 1615-1635. https://doi.org/10.1016/j.dsr2.2008.04.025.

78. Steinberg, D. K., Stamieszkin, K., Maas, A. E., Durkin, C. A., Passow, U., Estapa, M. L., et al., The outsized role of salps in carbon export in the subarctic Northeast Pacific Ocean. *Glob, Biogeochem. Cyc.*, **37**, e2022GB007523. https://doi.org/10.1029/2022GB007523, (2023).

79. Maas A.E., H. Gossner, M.J. Smith, L. Blanco-Bercial, Use of optical imaging datasets to assess biogeochemical contributions of the mesozooplankton. *J. Plank. Res.,* **43**, 475–491, (2021).

80. Motoda, S., Devices of simple plankton apparatus. Memoirs of the Faculty of Fisheries Hokkaido University 7: 73-94, (1959).

81. Gorsky, G., M. D. Ohman, M. Picheral, S. Gasparini, L. Stemmann, et al., Digital zooplankton image analysis using the ZooScan integrated system. *J. Plankt. Res*. **32**, 285-303. https://doi.org/10.1093/plankt/fbp124, (2010).

82. Vandromme, P. L. Stemmann, C. García-Comas, L. Berline, G. Gorsky, Assessing biases in computing size spectra of automatically classified zooplankton from imaging systems: A case study with the ZooScan integrated system. *Meth. Oceanogr.*, **1-2**. 3-21. https://doi.org/10.1016/j.mio.2012.06.001, (2012).

83. Visser, A., 2001, Hydromechanical signals in the plankton. *Marine Ecology Progress Series*, 222:1–24.

Acknowledgements:

We would like to acknowledge support from the NASA Ocean Biology and Biogeochemistry program, the National Science Foundation Biological and Chemical Oceanography programs and the Woods Hole Oceanographic Institution's Ocean Twilight Zone study. We greatly acknowledge the cooperation, skill and commitment of the Captains, Crews, Research Technicians and Administrative Staffs of the RRS James Cook (JC214), RRS Discovery (DY130 & DY131) and the R/V Sarmiento de Gamboa (SG2105) for making the EXPORTS-NA field deployment a reality. Special thanks to Laura Lorenzoni (NASA HQ), Mike Sieracki (formally NSF BIO-OCE), Paula Bontempi (formally NASA HQ), and Quincy Allison and his team (ESPO - NASA AMES) for their vision and support throughout the development and implementation of the

EXPORTS field campaign. Last, we like to thank our many EXPORTS colleagues for their brilliance, energy, dedication, hard work, support, and collegiality.

Data Availability:

All EXPORTS data used here is archived at NASA's SeaWiFS Bio-optical Archive and Storage System (SeaBASS) under the EXPORTS Experiment (https://seabass.gsfc.nasa.gov/experiment/EXPORTS). Data collected during the EXPORTSNA field expedition onboard the Sarmiento the Gamboa was archived under the OTZ_WHOI experiment (10.5067/SeaBASS/OTZ_WHOI/DATA001) and cruise name SG2105. The intercalibrated UVP particle size distribution data set presented here is available at https://doi.org/10.31223/X58709. To find out information about all the data collected during the EXPORTS field campaigns, their data repositories and availability, please visit: https://sites.google.com/view/oceanexports/home.

Supplementary Information:

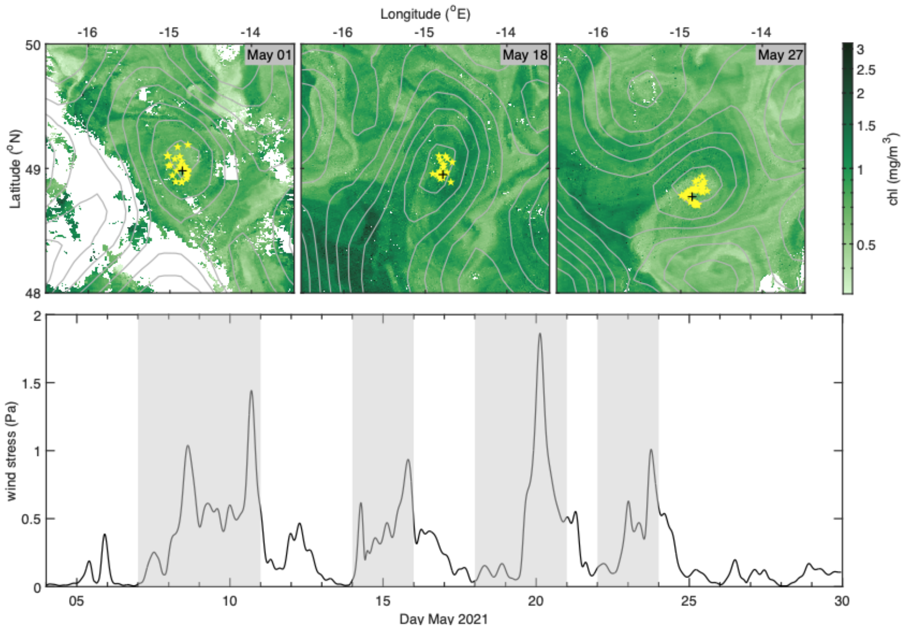

Fig S1 - Satellite Chl and SSH of the eddy field with track of Lagrangian float and wind stress time series showing ship work stoppages.

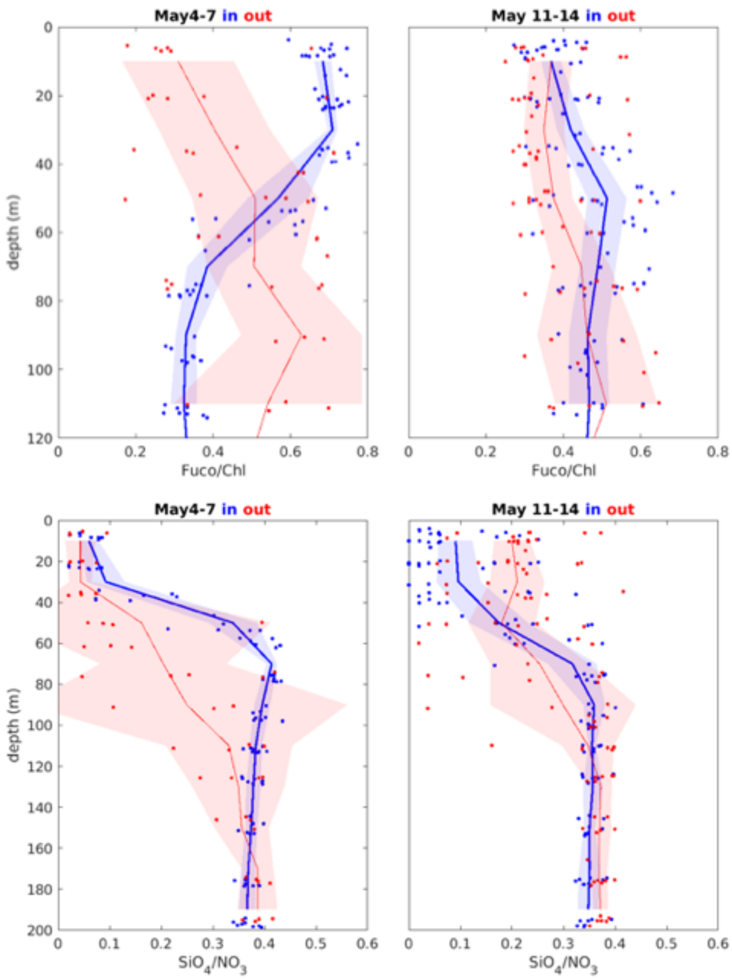

Supplemental Figure 2 - Vertical profiles of ratios of the fucoxanthin (biomarker pigment for diatom abundances) to total chlorophyll a concentrations (Fuco/Chl) and the silicate to nitrate concentrations (SiO_4/NO_3) in the eddy (blue) and outside the eddy (red) both before (May 4-7) and after (May 11-14) the first large storm. In the eddy is defined as stations located within 15 km of the analyzed eddy center and outside of the eddy is defined as those stations that are 15 to 60 km from the eddy center.

Table S1: Integrated POC and Particle Volume Inventories and Fluxes During Trap Deployments

Trap deployment	**Units**	**1**	**2**	**3**
Dates		May 5-11	May 12-15	May 22-24
Integrated NPP	mmolC m^{-2} d^{-1}	119	120	53
Integrated POC	mmolC m^{-2}	829	812	788
POC Turnover Time by NPP	day	7.0	6.7	14.9
Trap Type & Depth		75 m STT	75 m STT	105 m NBST
POC export	mmolC m^{-2} d^{-1}	11	9	22
e-ratio	-	0.09	0.08	0.41
POC Turnover Time by Export	day	75	90	36
Integrated Particle Volume	ml m^{-2}	421	1366	1279
Particle Volume Flux @ 100 m	ml m^{-2} d^{-1}	69	435	1273
Particle Volume Turnover Time	day	8.2	3.3	1.1

Notes: Determinations of water column integrated NPP rates from Table 1 in ref. (23) are averaged over the periods of the three trap deployment periods. Integrated POC stocks were calculated from available POC profiles water samplings profiles and averaged over the periods of the three trap deployments. Integrated POC export fluxes are determined using the shallowest depths available (Fig. 4b). E-ratios are calculated as the POC export flux at the base of the euphotic zone normalized by the NPP rate. Upper 100 m particle volume inventories and fluxes are calculated as in Figure 3d. Turnover times are calculated as the integrated POC or particle volume inventory in the upper 100 m divided by the export flux or for POC divided by NPP. STT is surface tethered trap array and NBST is Neutrally Buoyant Sediment Trap.

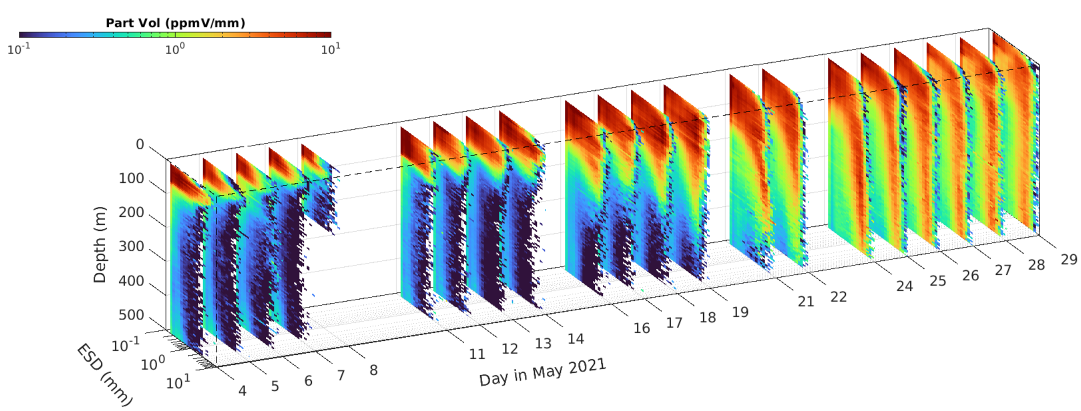

Figure S3: Daily mean profiles of the particle volume spectra (ppmV/mm) for all days during EXPORTS NA both within 15 km to the eddy center.

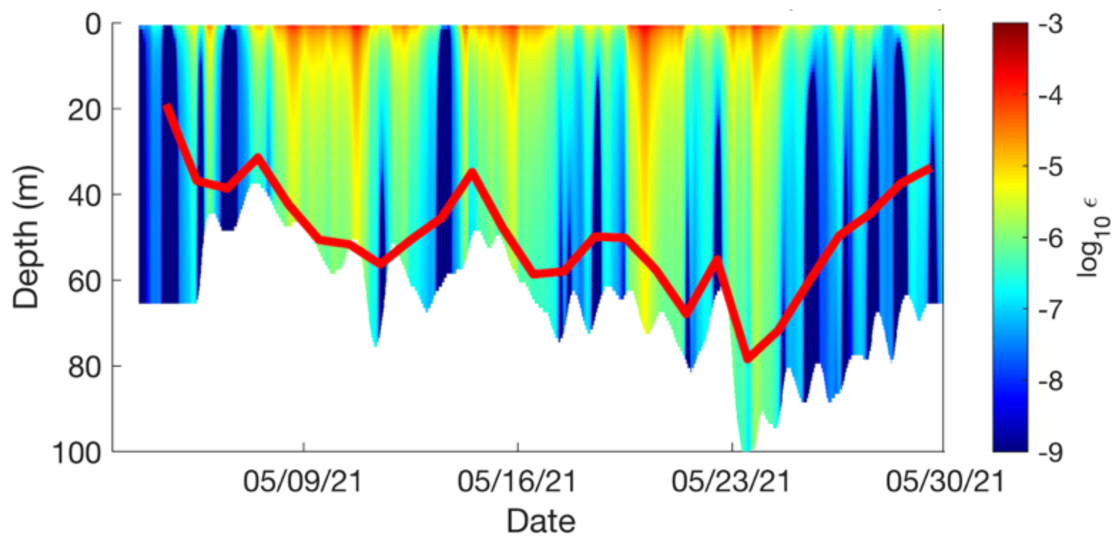

Figure S4: Upper layer contour of KE_Diss from air-sea flux scaling relationships. Daily mean mixed layer depth is shown in the solid red line.

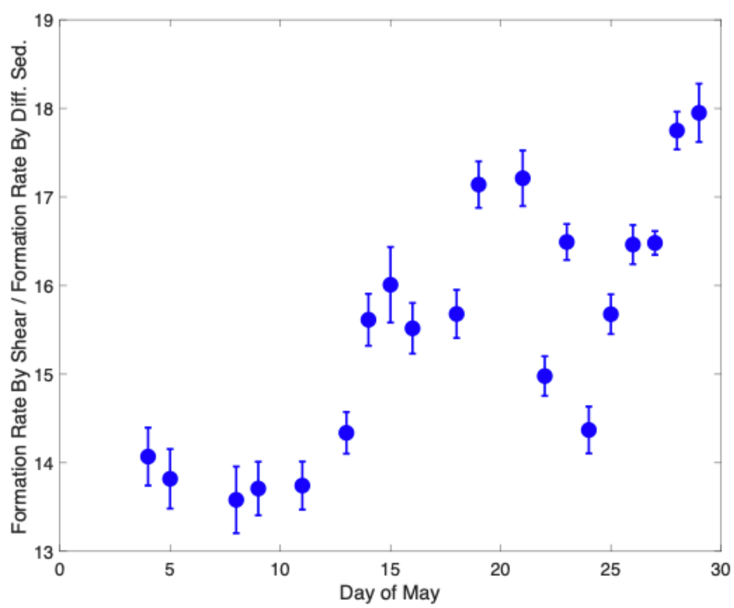

Figure S5: The ratio of large (> 5 mm) particle formation rate by turbulent shear to that by differential sedimentation for particles in the 40–80 m depth-range.

Table S2: Normalized Large Particle-Zooplankton Encounter Rates for the Mesopelagic

	Zooplankton Abundances (# m^{-2})			Large (D> 0.51 mm) abundances (# m^{-3})			Normalized Encounter Rates		
Depth Interval (m)	May 17	May 26	May 17	May 17	May 17	May 26	May 11	May 17	May 26
200-300	10236	23243	2.0	2.0	2.0	23243	5.21×10^{3}	1.24×10^{4}	7.88×10^{4}
300-400	20724	23528	0.9	0.9	0.9	23528	3.58×10^{3}	4.30×10^{4}	6.34×10^{4}
400-500	18333	21585	0.6	0.6	0.6	21585	3.54×10^{3}	3.01×10^{4}	4.75×10^{4}

Notes: Large particles are defined as those with D > 0.51 mm and zooplankton abundances are averaged from paired day-night tows (see *Methods*). Encounter rates are available for May 11, 17 and 26, all normalized to the vertical profile on May 11.